Control of Doubly Fed Asynchronous Generators for Wind Power Applications

University of Bergen

By: Jakob Birkenes

June 1, 2021

Abstract

This thesis researches and develops a Doubly Fed Induction Generator (DFIG) model suitable for a university lab environment. DFIGs have attracted significant amount of research, as it is one of the leading generator systems for wind power. The hardware is based on intelligent power modules from Fuji along with a Texas Instruments microcontroller which controls the insulated gate bipolar transistors (IGBT). Printed Circuit Boards (PCB) has been developed for the converter and measurement circuits. The lab generator is a 1.1 kW induction motor from Terco with slip rings connected to the rotor. The converter uses field-oriented control to control the performance of the generator, and samples signals required for the control system. This includes currents, voltages, rotor position and speed through an incremental encoder. And for future lab test a simulation of a DFIG have been done to use as a reference when tests are done on real hardware. In the end there is a discussion about which steps one should take forward, and which aspects that can be improved upon.

Acknowledgements

This master's thesis in Electrical Power Engineering is the end of my six year long education and marks the start of my professional career at Equinor. I would like to thank the University of Bergen and the Western Norwegian University of Applied Science for facilitate my education and making it a worthwhile experience.

I wish to thank my thesis advisor, Associate Professor Shujun Zhang for his help and support throughout this special pandemic year, where many things became increasingly difficult. From his advice I was exposed to many new ideas and concepts I would not have thought of otherwise.

I would also like to mention Professor Martin Fernø from the University of Bergen for being my co-advisor. Unfortunately, we only got in contact the final month, but the advice I was given was appreciated.

Eirik Haustveit deserves a special thank you for being a reliable source for help and ideas this year. Many aspects of this thesis was new to me when I started and the advice I was given was helpful.

Finally, I would like to thank my fellow master's students who have been an important social outlet in a year where things have otherwise been very quiet.

Contents

List of Figures

List of Tables

Chapter 1

Introduction

As global warming becomes a more pressing issue, the interest in renewable energy sources has only increased. Wind power, while being one of the oldest sources of energy has only gotten more widespread in recent years. This is because prices are lower than ever and countries have to increase their renewable energy production to meet requirements from targets set by the 2015 Paris agreement. From 2010 to 2019, installed wind energy capacity increased by over three times worldwide, and it has shown no sign of slowing down as more companies are getting familiar with the technologies. [1][2]

It has also become more common to place turbines at sea which has allowed for significantly larger turbines with higher capacity. For example, Equinor is planning to use 14MW turbines for their Dogger Bank wind farm project in the North Sea. [3]

Different generator concepts has been used in wind turbines throughout history, but the dominant type in recent years has been the Doubly Fed Induction Generators (DFIG). While other generator concepts have to work at a fixed speed in order to maintain correct frequency for the grid, the DFIG can operate at a varied speed which is a huge advantage as wind speed is unpredictable. The DFIG is also versatile in that it can regulate how much reactive power it produces which makes it a useful asset on weaker grids where conditions are not stable. This makes DFIGs a worthwhile research field in order to meet the varied tasks and problems that can arise when using DFIG wind turbines. [4]

1.1 Purpose of the thesis

This thesis will aim to research and design the core components of the DFIG in order to do future laboratory tests at the Western Norwegian University of Applied Sciences. The system is designed for the generator to operate at both sub and super synchrounous speeds through the use of an induction motor which will simulate the torque of a real turbine. The torque generating induction motor will be controlled through a frequency converter. This will make it possible to do a multitude of different tests in the future. The resulting lab model will be an assett for testing a generator suitable for wind power.

1.2 Structure of the thesis

The thesis is divided into chapters covering different parts of the DFIG system. Chapter 3 goes into the theory behind the DFIG and which components are important when building and operating one. It also looks into the most important feature of the controller and how it functions. Chapter 4 describes the objectives of the project and which components that will be designed. Chapter 5 describes the design process of the main components to the DFIG and the Printed Circuit Boards (PCB) that has been designed as a result. Chapter 6 is the result of the simulations that have been done using the control system and the circuit boards that have been made and soldered for the university lab. Chapter 7 will be a discussion of the work and result done and about future work related to this project.

Chapter 2

Wind Turbine Generator Systems

Multiple wind turbine generator systems have been implemented throughout history and has dramatically changed the last 30 or so years. The biggest advancements has been in the types of generator, power electronics, speed controllability and the way the aerodynamic power is limited. The most common turbines in the late 20th century were fixed speed turbines which had some issues. Mainly that you needed to compensate for the reactive power from the asynchronous generator, but also the mechanical stresses on the generator were higher and wind fluctuations were creating power fluctuations on the grid. Some iterations to improve this design was developed, mainly one with a variable rotor resistance which allowed the turbine speed to be more variable, which contributed to mechanical stress relief and smoother electrical output. It did however have a consistent power loss through the rotor resistance which reduced the power it could output. In recent years systems which allows for variable speed has be developed. One of the methods is using a full scale power converter between the grid and the turbine, or the DFIG which is the main topic of interest in this thesis.[4]

2.1 Doubly Fed Induction Generators

Doubly fed induction generators are machines that have attracted great research interest with the maturing of wind power technologies. Traditionally slip ring machines were common, but in recent years brushless machines have become standard as brushless machines have fewer moving parts and are

therefore more reliable. This is a major advantage as higher uptime equals more power produced. It is also a significant advantage in offshore applications where service costs are higher. Modern brushless DFIGs are designed with two separate stator windings where the winding with the most poles are connected to the grid via two converters allowing bidirectional power flow. [5]

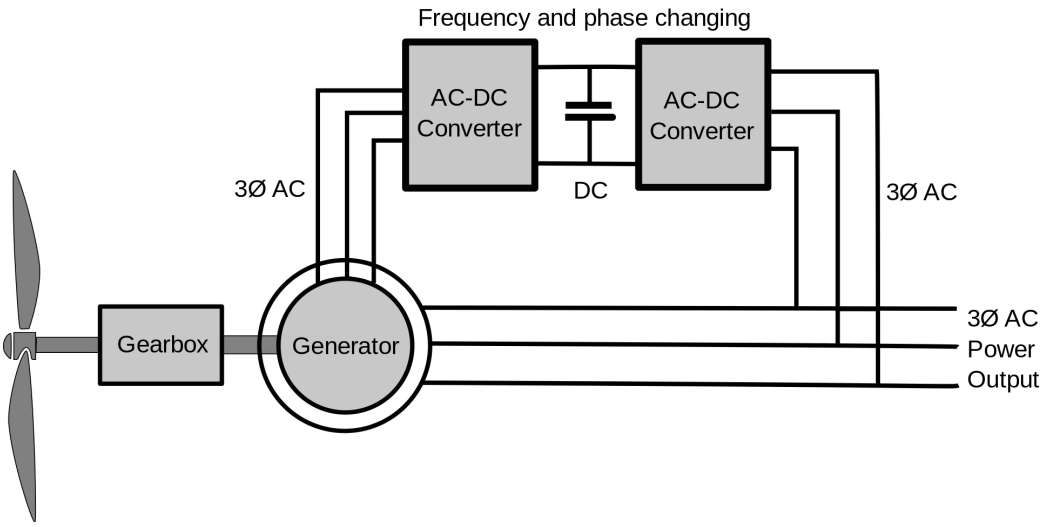

Figure 2.1: Doubly fed induction generator principle [6]

The main benefit of a DFIG is its ability to operate at various levels of speed with high efficiency while supplying a constant voltage and frequency. This is an advantage for the grid as it provides more flexibility in the power generation and a more stable frequency and voltage. The bidirectional power flow into the rotor is what allows power production to happen at both super-synchronous and sub-synchronous speeds. Neglecting losses, rotor power can be represented using slip [7]

$$P_{rotor} \simeq -sP_{stator} \tag{2.1}$$

$$P_{stator} \simeq \frac{P_{mec}}{1-s} \tag{2.2}$$

And the mechanical power is represented as:

$$P_{mech} \simeq P_{stator} + P_{rotor} \tag{2.3}$$

The rotorcurrents frequency can be expressed as

$$f_2 = f_1 - \frac{n_2 \cdot p}{60} \tag{2.4}$$

where f_1 is the stator current frequency in Hz, f_2 is the rotor current frequency, n_2 is the mechanical rotations per minute and p is the DFIGs pole pairs. [5]

Normally induction machines have their rotor short circuited shown in figure 2.2, but since DFIGs have their rotor connected to the grid through the converters, the equivalent circuit looks like figure 2.3.

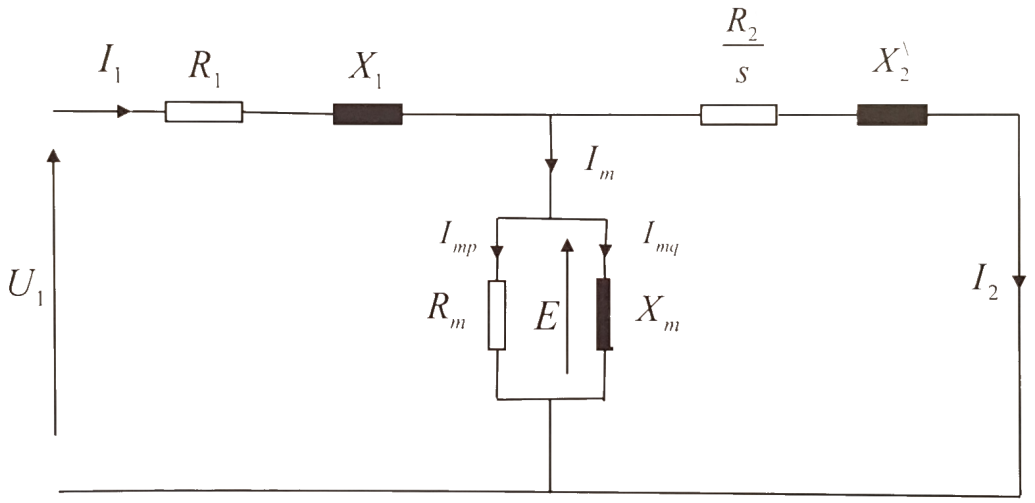

Figure 2.2: Equivalent circuit for induction machine with a short-circuited rotor.[5]

Applying Kirchoff's voltage law to the circuit in figure 2.3 gives [7]

$$V_s = R_s I_s + j\omega_1 L_{s\lambda} I_s + j\omega_1 L_m (I_s + I_r + I_{R_m}) \tag{2.5}$$

$$\frac{V_r}{s} = \frac{R_r}{s} + j\omega_1 L_{r\lambda} I_r + j\omega_1 L_m (I_s + I_r + I_{R_m}) \tag{2.6}$$

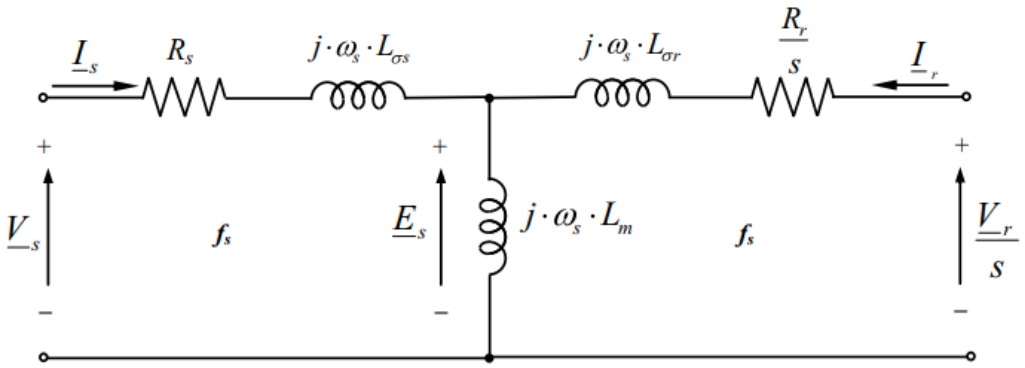

Figure 2.3: Steady state equivalent circuit for induction machine with a non short circuited rotor.[7]

From here we get the stator, rotor and air gap flux

$$\psi_m = L_m(I_s + I_r + I_{R_m}) \tag{2.7}$$

$$\psi_s = L_{s\lambda} I_s + L_m(I_s + I_r + I_{R_m}) = L_{s\lambda} I_s + \psi_m \tag{2.8}$$

$$\psi_r = L_{r\lambda} I_r + L_m(I_s + I_r + I_{R_m}) = L_{r\lambda} I_r + \psi_m \tag{2.9}$$

From here equation 2.5-2.6 becomes

$$V_s = R_s I_s + j\omega_1 \psi_s \tag{2.10}$$

$$\frac{V_r}{s} = \frac{R_r}{s} I_r + j\omega_1 \psi_r \tag{2.11}$$

$$0 = R_m I_{rm} + j\omega_1 \psi_m \tag{2.12}$$

Equations [2.10 - 2.12] are accurate in steady state and from them you can derive phasor diagrams for any operating condition. They are however not suitable for controlling the machine. To control the machine some changes have been made including changing the reference frame of the motor to a rotating one which simplifies the process. Changing the reference frame from a stationary one to a rotating one makes it so alternating signals can be treated as constant DC signals. [7]

2.1.1 Space Vectors

Space vector notation is a way to represent flux, voltage, and current magnitude in AC machines. By treating these magnitudes as a single vector, it is possible to derive equations that represent their behavior in an easier way than the standard three-phase representation. For controlling AC machines we have different reference frames that represent these space vectors that will be discussed in chapter 2.1.2. Figure 2.4 shows the different reference frames adding up to a common space vector.[7]

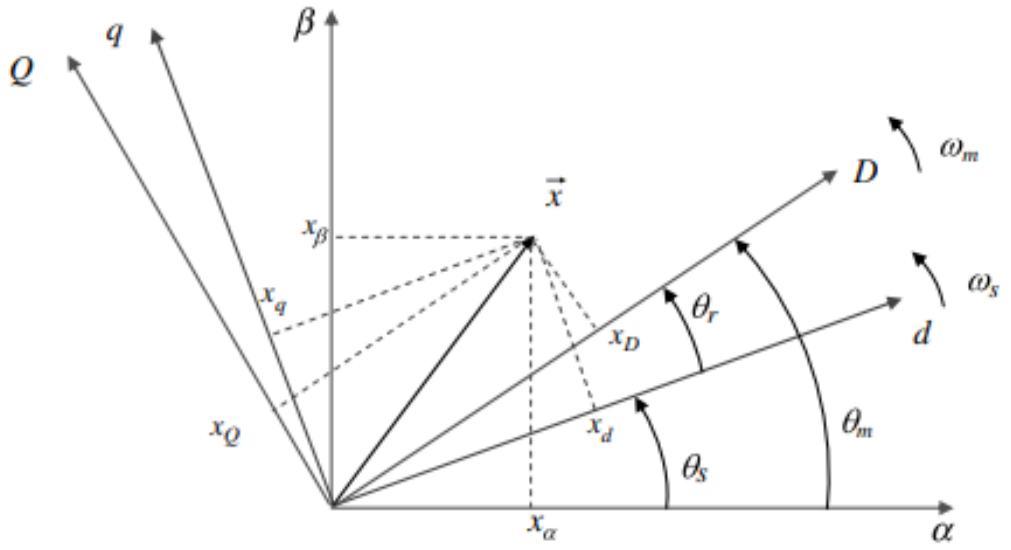

Figure 2.4: Space vector representation in different reference frames where DQ and dq are rotating ones while $\alpha\beta$ is stationary.[7]

2.1.2 $\alpha\beta$ and dq reference frame

The Clarke transformation shown in equation 2.13 is used to convert a three phase system into a two phase state vector representation of the voltages. These alpha beta voltages are converted into a rotating reference frame called a direct quadrature or dq reference frame using equation 2.14. [7]

$$\begin{bmatrix} v_\alpha \\ v_\beta \end{bmatrix} = \frac{2}{3} \begin{bmatrix} 1 & -\frac{1}{2} & -\frac{1}{2} \\ 0 & \frac{\sqrt{3}}{2} & -\frac{\sqrt{3}}{2} \end{bmatrix} \cdot \begin{bmatrix} v_a \\ v_b \\ v_c \end{bmatrix} \tag{2.13}$$

$$\begin{bmatrix} v_d \\ v_q \end{bmatrix} = \begin{bmatrix} cos\theta & sin\theta \\ -sin\theta & cost\theta \end{bmatrix} \cdot \begin{bmatrix} v_\alpha \\ v_\beta \end{bmatrix} \tag{2.14}$$

Once the regulator has changed the dq voltage magnitudes, the transformation can be done inversely to return to the real sinusoidal values. The inverse transformations can be shown in equation 2.15 and 2.16.

$$\begin{bmatrix} v_a \\ v_b \\ v_c \end{bmatrix} = \begin{bmatrix} 1 & 0 \\ -\frac{1}{2} & \frac{\sqrt{3}}{2} \\ -\frac{1}{2} & -\frac{\sqrt{3}}{2} \end{bmatrix} \cdot \begin{bmatrix} v_\alpha \\ v_\beta \end{bmatrix} \tag{2.15}$$

$$\begin{bmatrix} v_\alpha \\ v_\beta \end{bmatrix} = \begin{bmatrix} cos\theta & -sin\theta \\ sin\theta & cost\theta \end{bmatrix} \cdot \begin{bmatrix} v_d \\ v_q \end{bmatrix} \tag{2.16}$$

Applying these transformations to the equivalent model simplifies it further as shown in 2.5. With the $\alpha\beta$ model one can calculate the stator and rotor electric power, as well as electromagnetic torque as shown in equations [2.17 - 2.20]. These equations are also equivalent to the dq equations where you replace α with the d-axis and β with q-axis for the same result.[7]

$$P_s = \frac{3}{2} Re\{\vec{v}_s \cdot \vec{i}_s^*\} = \frac{3}{2}(v_{\alpha s} i_{\alpha s} + v_{\beta s} i_{\beta s}) \tag{2.17}$$

$$P_r = \frac{3}{2} Re\{\vec{v}_r \cdot \vec{i}_r^*\} = \frac{3}{2}(v_{\alpha r} i_{i\alpha r} + v_{\beta r} i_{\beta r}) \tag{2.18}$$

$$Q_s = \frac{3}{2} Im\{\vec{v}_s \cdot \vec{i}_s^*\} = \frac{3}{2}(v_{\beta s} i_{\beta s} + v_{\alpha s} i_{\alpha s}) \tag{2.19}$$

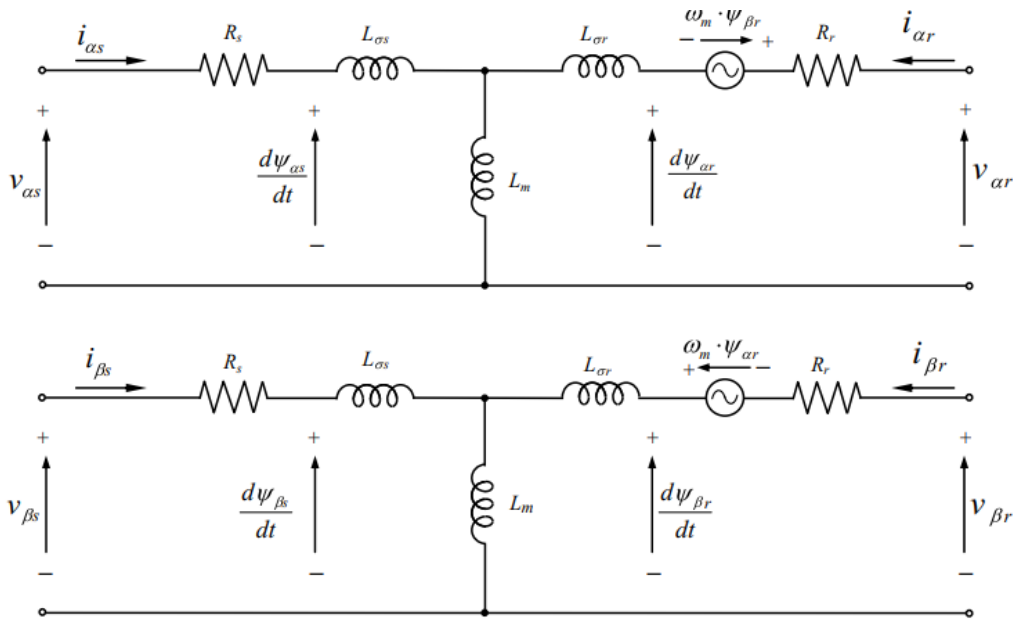

Figure 2.5: Equivalent circuit for DFIG after Clarke transformation.

$$Q_r = \frac{3}{2} Re\{\vec{v}_r \cdot \vec{i}_r^*\} = \frac{3}{2}(v_{\beta r} i_{i\beta r} + v_{\alpha r} i_{\alpha r}) \tag{2.20}$$

From this equivalent circuit shown in figure 2.6, we can derive formulas that are useful for the control of the machine. For the stator side we have:

$$v_{ds} = R_s i_{ds} + \frac{d\psi_{ds}}{dt} - \omega_s \psi_{qs} \tag{2.21}$$

$$v_{qs} = R_s i_{qs} + \frac{d\psi_{qs}}{dt} + \omega_s \psi_{ds} \tag{2.22}$$

$$\psi_{ds} = L_s i_{ds} + L_m i_{dr} \tag{2.23}$$

$$\psi_{qs} = L_s i_{qs} + L_m i_{qr} \tag{2.24}$$

And for the rotor side we have:

$$v_{dr} = R_r i_{dr} + \frac{d\psi_{dr}}{dt} - \omega_r \psi_{qr} \tag{2.25}$$

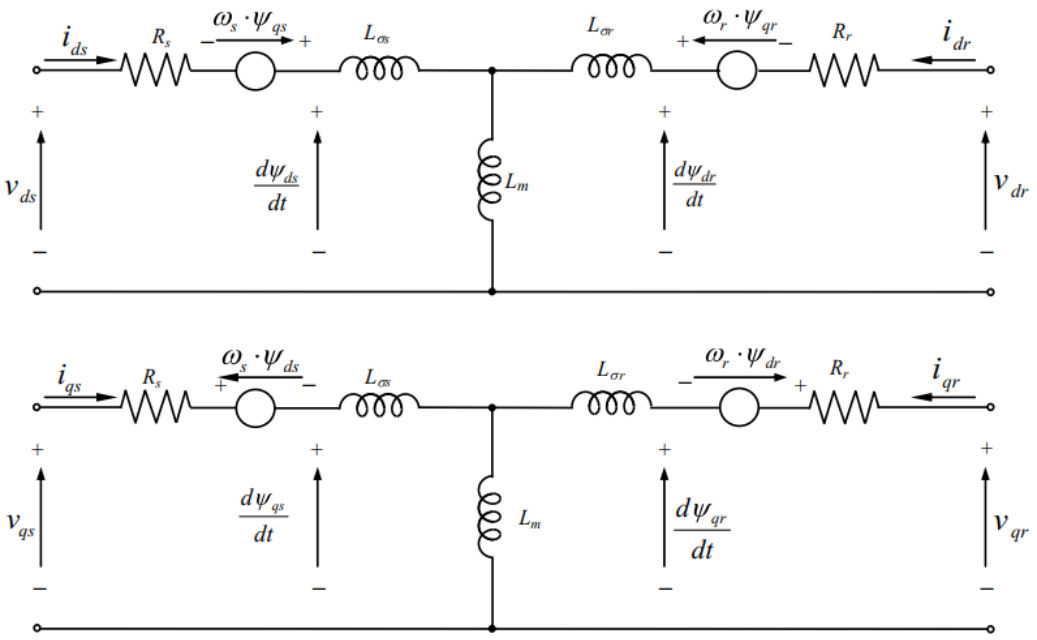

Figure 2.6: Equivalent circuit for DFIG after Park transformation.

$$v_{qr} = R_r i_{qr} + \frac{d\psi_{qr}}{dt} + \omega_r \psi_{dr} \tag{2.26}$$

$$\psi_{dr} = L_s i_{ds} + L_m i_{dr} \tag{2.27}$$

$$\psi_{qr} = L_s i_{qs} + L_m i_{qr} \tag{2.28}$$

2.2 Converter Control Systems

The rotor of the DFIG is fed through two full bridge transistor units containing twelve transistors total as shown in figure 2.7. A full bridge allows power to flow in both directions which is necessary for the DFIG to operate at a wide range of torque. The DC link between the converters gets the voltage smoothed by a large capacitor. The gate of each transistor is connected to a PWM-signal generated by a controller. The controller uses measurements from the circuit and motor to control and regulate the converters until the generator has a desired output.

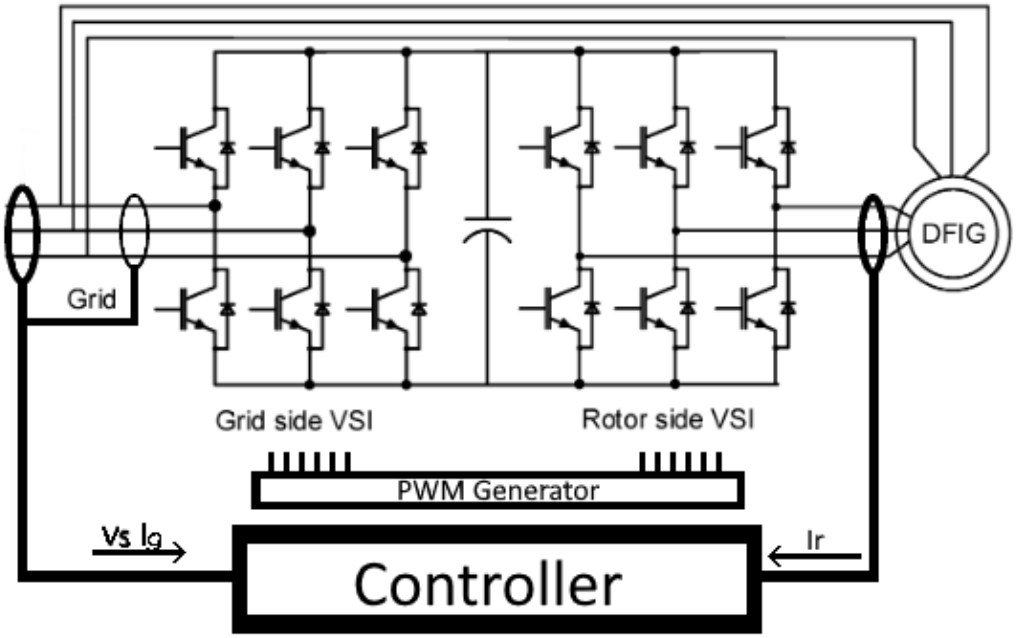

Figure 2.7: Full bridge converters for DFIG rotor. Adapted from [8]

2.2.1 Variable Switch Inverter

An active front end or full bridge converter consists of six insulated-gate bipolar transistors (IGBT), where each leg of the converter consists of two IGBTs each connected in anti-parallel with a flyback diode. A more detailed image of the converter can be shown in figure 2.8. The flyback diode gives a path for voltages induced by inductive loads. These voltage spikes can be quite large because the switching frequencies are often several kHz, and the voltage spikes are dependent on the rise time of the current across the inductor $V_L = L\frac{di}{dt}$. The transistors are controlled by a PWM (Pulse Width Modulation) signal S_{a-c} which decides the duty cycle of its respective transistor. The capacitor C_d shown in figure 2.8 reduces the ripple voltage of the DC bus. While there exists multiple topologies for rectifying current like thyristors and diode bridges, they are not useable for this operation as you require a bidirectional power flow.

The total current through the converter can be represented with equation 2.29. This duty cycle will not remain constant but will follow the controller's

regulation to achieve the desired DC-bus voltage.

$$S_a i_a + S_b i_b + S_c i_c = C\frac{dv_{dc}}{dt} + i_{load} \tag{2.29}$$

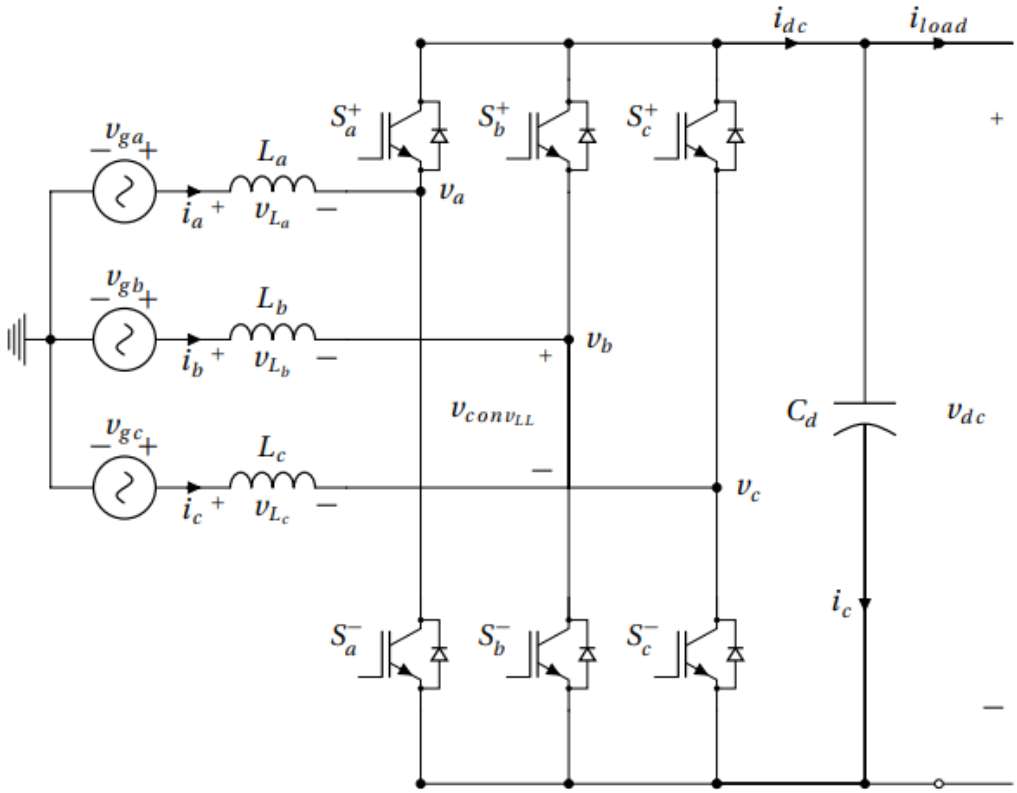

Figure 2.8: Active front end converter controlled by PWM signals S_{a-c} where the gate signals on the same transistor leg are inverted to prevent them from being on at the same time.[9]

2.2.2 Sinusoidal PWM

One of the most common modulation techniques in power electronics is sinusoidal PWM where you compare a triangular signal to a reference signal. If the triangular signal is higher than the reference signal it creates output voltage. An example of a PWM reference and triangle signal is shown in figure 2.9 where the triangle signal has a frequency of 20 times the reference

signal. The IGBT will output voltage if the conditions in equation 2.30 are met. [7]

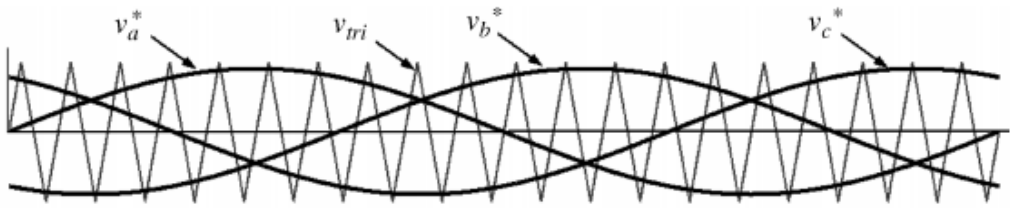

Figure 2.9: PWM generation signal [7]

$$S_j = 1 \;\; if \; v_j^* > v_{tri} \;\; with \;\; j = a, b, c \tag{2.30}$$

$v_{a,b,c}$ = reference signal for each phase

v_{tri} = triangular signal

An important index for PWM modulation is the frequency modulation index (m_f) shown in equation 2.31. This index is the relation between the frequencies of the triangular signal and the reference signal. The higher this index is, the cleaner the output signal will be. [7]

$$m_f = \frac{f_{tri}}{f_{ref}} \tag{2.31}$$

The frequency f_{tri} does however also determine the switching frequency, and depending on which component is used, it might restrict the switching frequency. With a higher switching frequency, you also get higher switching losses, so finding a balance between these factors is important.

Another index that is important is the amplitude modulation index (m_a) which is the relationship between the amplitude of the reference signal and the triangular signal. This index is expressed by equation 2.32. [7]

$$m_a = \frac{|v^*|}{|v_{tri}|} \tag{2.32}$$

If m_a is above 1 overmodulation happens and detecting the sine wave becomes hard. The relationship between the fundamental output voltage and the DC voltage is given by 2.33.

$$v_{an} = m_a \cdot \frac{V_{bus}}{2} \quad if \quad m_a \leq 1 \tag{2.33}$$

This PWM technique is referred to in literature as unipolar PWM and is limited in comparison to PWM with third harmonic injection. [7]

2.2.3 SVPWM with third harmonic injection

PWM with third harmonic injection is a small modification which allows for a higher amplitude of the output signal with no loss of quality. Third harmonic injection means that a second sine wave with a frequency three times the fundamental frequency is added to the main signal. In figure 2.10 we can see that the third harmonic signal V_3 has a positive peak at $\pi/4$ and at $\frac{3\pi}{4}$ which increases the reference signal and creates two new maximums at $\theta = \frac{\pi}{3} \quad and \quad \frac{2\pi}{3}$. The negative peak of the third harmonic happens at $\pi/2$ which means the peak of the reference signal is reduced. [7]

Using third harmonic injection the linear modulation region is increased from 2.34 to 2.35 increasing the fundamental output volage amplitude 1.15 times.

$$Normal \ \ linear \ \ modulation \ \ region: \ \ 0 \leq m_a \leq 1 \tag{2.34}$$

$$Adjusted \ \ linear \ \ modulation \ \ region: \ \ 0 \leq m_a \leq 1.15 \tag{2.35}$$

2.3 Control Algorithms

This section will go into detail about the vector control algorithm programmed in Simulink that will be used for the simulation and for the lab experiments. In this chapter vector control of DFIG will be covered as it is the most studied and established method. The algorithm or control strategy implements the theory from chapter 2.2 in simulink, along with concepts such as PI regulators and maximum power point tracking (MPPT). Figure 2.12 shows the control system for the rotor converter which most notably shows

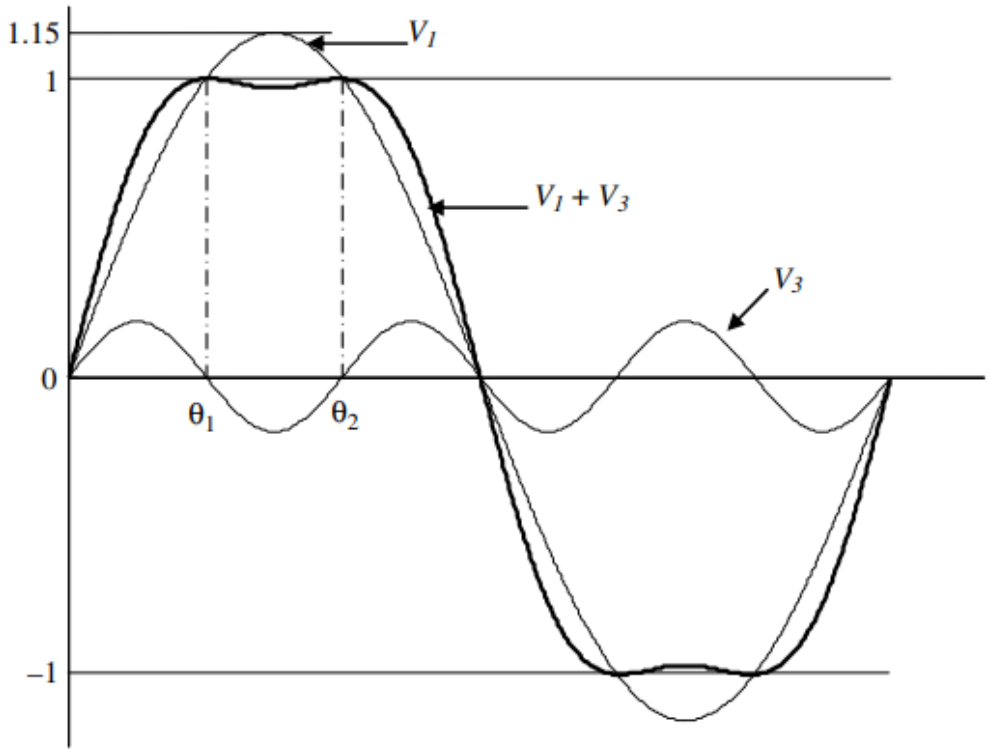

Figure 2.10: Reference signal peak lowered by third harmonic voltage injection.[7]

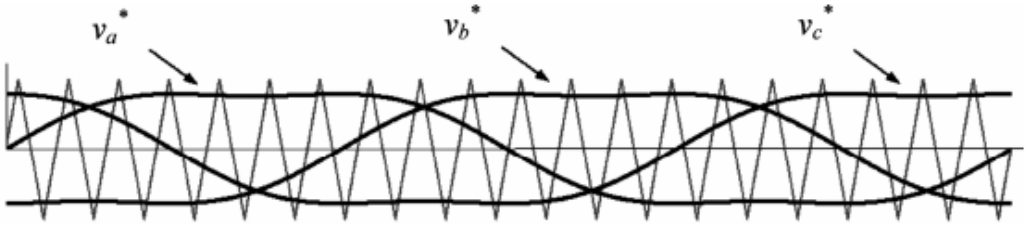

Figure 2.11: PWM generation signal with third harmonic injection.

the regulators for the dq components of the current and speed regulator for the shaft.

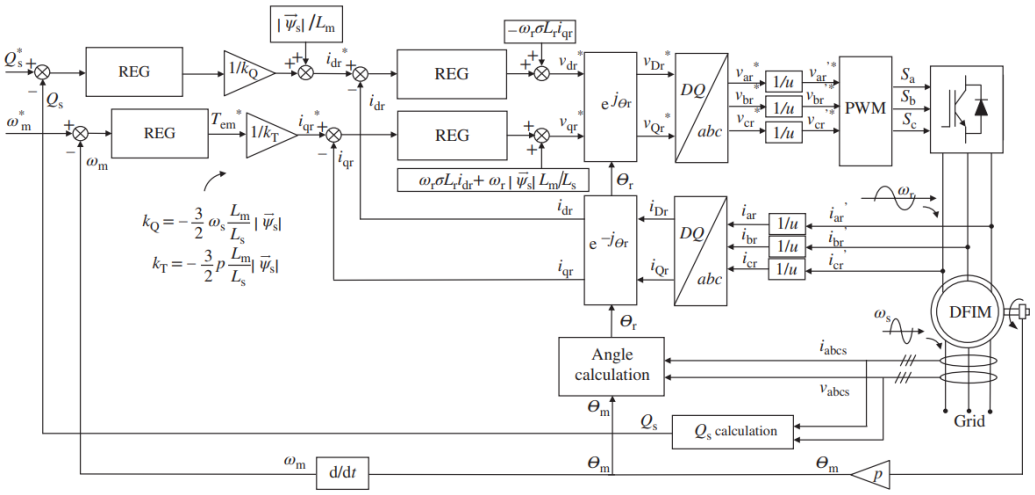

Figure 2.12: Complete vector control system of DFIG. [4]

2.3.1 Maximum power point tracking

In region two of figure 2.13 the objective of the speed controller is to extract as much power as possible from the windmill. There are several methods for MPPT which have a varying level of accuracy.

Indirect speed control

This method is an easy form of control which uses the idea that the wind turbine is dynamically stable around the maximum power point, and that the variable speed turbine naturally goes back to its operating point. Referring to figure 2.14, the maximum power point you find along the curve that intersects point a and c. When the wind speed increase or decrease, the operating point gets raised vertically along the arrows, and it will deviate from the maximum efficiency point. The controller then provides the electromechanical torque corresponding maximum power point, which makes the turbines rotational speed increase or decrease until it hits an equilibrium point. [7]

When the turbine is working at the maximum power point,

$\lambda_{opt} = \frac{R\omega_t}{V_v}$, $C_p = C_{p\_max}$ and $C_t = C_{t\_opt}$

The aerodynamic torque extracted by the turbine is given by equation 2.36

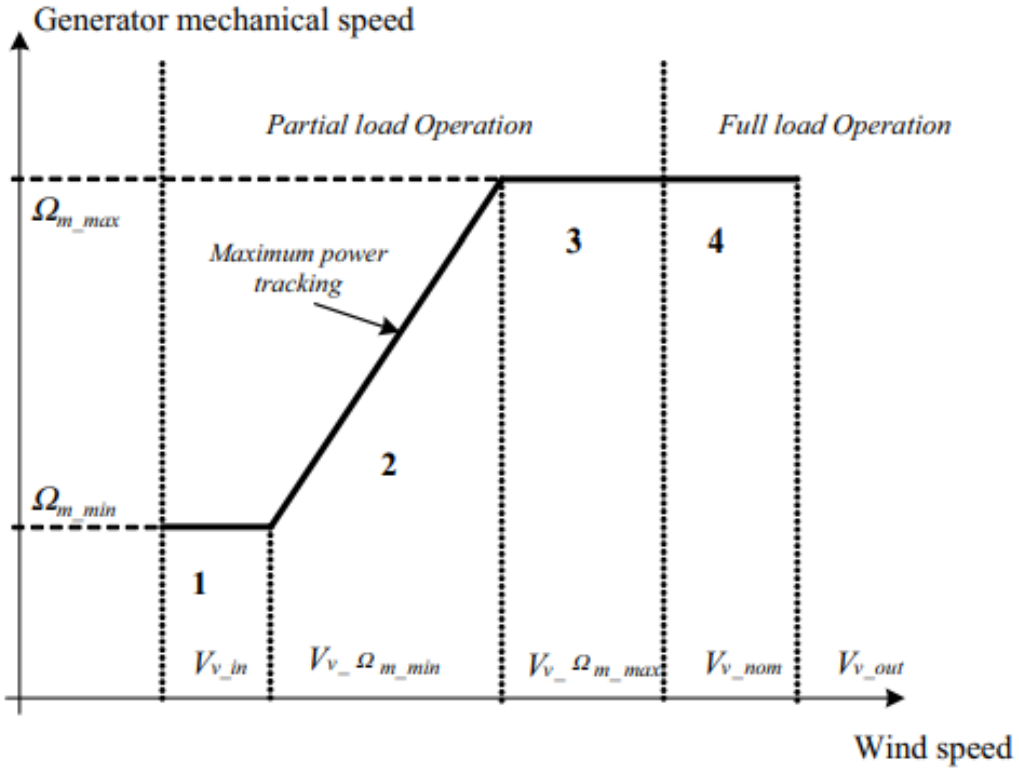

Figure 2.13: Control regions of a wind turbine.[7]

$$T_t = \frac{1}{2}\rho\pi R^3 \frac{R^2\omega_t^2}{\lambda_{opt}^2}\frac{C_{p\_max}}{\lambda_{opt}} \tag{2.36}$$

$$T_t = \frac{1}{2}\rho\pi \frac{r^5}{\lambda_{opt}^3} C_{p\_max}\omega_t^2 = k_{opt\_t}\omega_t^2 \tag{2.37}$$

which simplifies to

$$k_{ops\_t} = \frac{1}{2}\rho\pi \frac{R^5}{\lambda_{opt}^3} C_{p\_max} \tag{2.38}$$

where the k_{opt_t} variable is the one used in the control algoritm in figure 2.15.

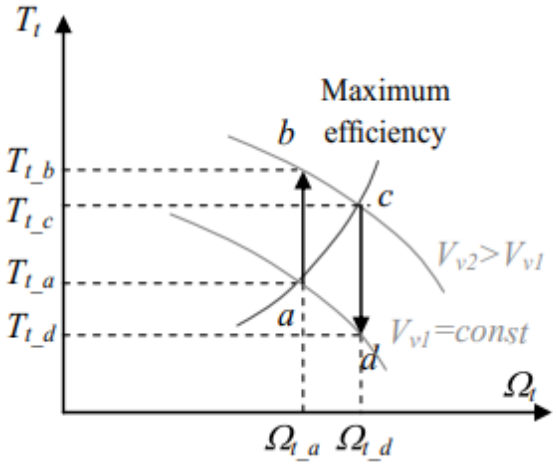

Figure 2.14: Maximum power point tracking curve based on torque and speed of the turbine. [7]

This gives a control system which looks like the one in figure 2.15. The most important part here is the branch with k_{opt} as it is the dominant one. In situations where the dampening is low D_{t_m} is negligible.

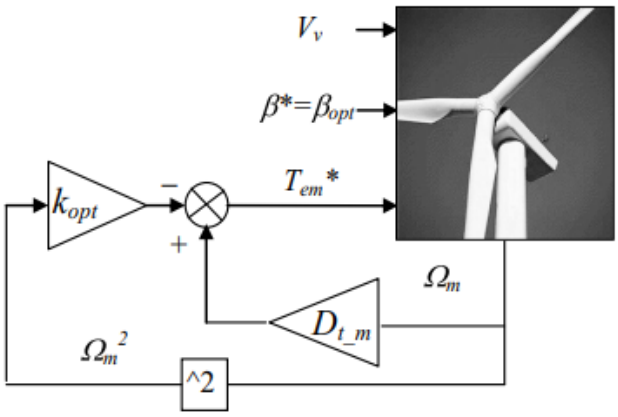

Figure 2.15: Indirect speed control[7]

Direct speed control

This method is faster and more responsive than the indirect version. The method estimates the aerodynamical torque and the value is used by the regulator to control the speed using equation 2.39. [7]

$$\omega_m^* = N\sqrt{\frac{T_{t\_est}}{k_{opt\_t}}} \tag{2.39}$$

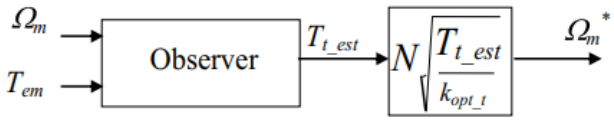

Figure 2.16: Direct speed control[7]

2.3.2 Angle estimation

Vector control of the DFIG requires estimation of the angle of the rotor of the machine. This can be estimated using a phase locked loop with an optical encoder. The angle needed for the control is θ_r in figure 2.4. From the optical encoder we find θ_m which is ahead of the d-axis by θ_r degrees. So, to get from the D-axis to the d-axis θ_s is subtracted from θ_m. From the steady state analysis we have equation 2.40 which if R_s is neglected because it is small, we get:

$$\vec{v_s} = R_s\vec{i_s} + \frac{d\vec{\psi_s}}{dt} \cong j\omega_s\vec{\psi_s} \tag{2.40}$$

From here if the R_s term is neglected in equation 2.41 and 2.42 we get the angle θ_s from 2.43

$$\psi_{\alpha s} = \int (v_{\alpha s} - R_s i_{\alpha s})dt \tag{2.41}$$

$$\psi_{\beta s} = \int (v_{\beta s} - R_s i_{\beta s})dt \tag{2.42}$$

$$\theta_s = tan^-1(\frac{\psi_{\beta s}}{\psi_{\alpha s}}) \tag{2.43}$$

From here we assume that the voltage space vector is 90° phase shifted from the stator flux, and subtract $\pi/2$ radians from the V_{abc} space vecotr and find an adequate estimate for ω_s when using 2.43. Then using equation 2.44 we can find the angle of θ_r. Figure 2.4 shows the angles that this method finds. [7]

$$\theta_m - \theta_s = \theta_r \tag{2.44}$$

2.3.3 PI Regulators

PI regulators are used to regulate a measured value towards some reference value. It has two branches which affect the regulation time and speed. The proportional component looks at the difference between the reference value and the measured value and gives a proportional amplification that seeks to reduce the gap between these two values. The integral component looks at the difference between the reference and measured value over time and eliminates minor differences if there is an error after the proportional component has stopped acting.

For applications that require a type of regulation with less overshoot and higher accuracy, a third derivative component can be used which works as a dampening component. The derivative component tries to predict the future trends based on the current change rate of the signal. In the case of regulating current loops for the DFIG, it is not necessary.

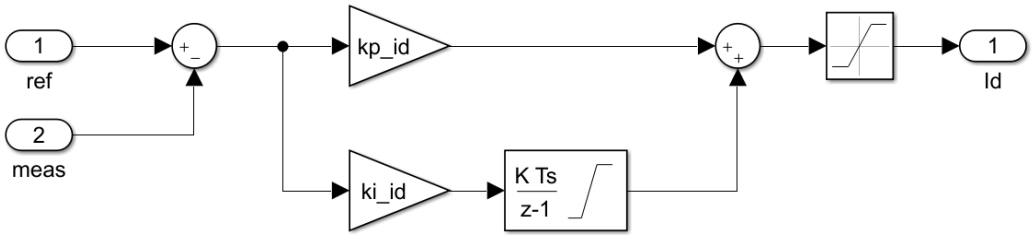

Figure 2.17: Example of PI regulator in Simulink with a discrete time integrator.

Chapter 3

Project Objectives

Designing a converter bridge for the DFIG is a challenge as there are several components to the converter itself. Some of the more theoretical aspects have been described in the previous chapter, but there are several problems that only arise when implemented on real hardware. Examples of problems like this are parasitic inductances, inaccuracy in measurements, controller hardware limitations and component accessibility. There are also challenges associated with the PCB design process whenever 230V or higher is used such as adequate spacing, path dimensions, solder difficulty when prototyping, component selections, capacitor types and filters.

The main components that has been developed for this report is:

- Simulation of DFIG developed in Simulink.
- Grid and rotor side IGBT converter PCB.
- Measurement PCB for 3-phase stator current and voltage.
- Measurement PCB for 3-phase rotor current.
- Rotor angle estimation with optical encoder.

The current measurement cards need to convert the current of each phase into a signal which can be used by the controller. The controller can sample signals in the ∼0-4V range, which means that the signal needs to be scaled appropriately so no signal exceeds the maximum rating and damages the control card. The maximum rating for sampled analog signals is between

-0,3V to 4,6V for the Texas Instruments board used in this project. The same thing needs to be done with the voltage measurements. [10]

The converters needs to have IGBTs and drivers that can be controlled by the controller. The DC bus needs to have an adequate capacitor size so that the DC voltage is smooth enough to not cause problems with the controller sampling the voltage. Ideally the circuit board will also be stackable with the control card making it a compact fit with less signal jumper wires, although in a prototype phase this is not something that is required.

Chapter 4

DFIG Simulation in Matlab and Simulink

Matlab is a programming and computing environment where one can create algorithms, user interfaces and visualization of programs that simulate real world applications. Simulink is an extension of Matlab which visualizes the programming itself allowing for programming using blocks representing models of components and systems or mathematical operations. It also allows running simulations of the programmed system. Simulation results are reported in 7. [11]

4.1 Steady State Analysis 1.1kW Lab Motor

In order to better understand what to expect from the lab motor one can simulate the steady state of the motor, one where $Q_s = 0$ and another where $i_{dr} = 0$. Two motor states are used in this program and the parameters are similar to the lab motor. The parameters are shown in figure 4.1. [12]

4.2 Dynamic Torque Test Program and Parameters

This simulation is to test the response to torque changes from the wind turbine onto the DFIG. The control system has been developed from theory in

General Motor and Converter Data 1.1kW		
Power	P_{mec}	1100
Stator voltage	V_s	230V
Stator current	I_s	5.5A
Rotor voltage	V_r	260V
Rated speed	ω_m	1440rpm
Rated torque	T_{em}	7.29Nm
Pole Pairs	P_P	2
Stator resistance	R_s	0.47Ω
Rotor resistance	R_r	0.34Ω
Stator and rotor inductance	L_s and L_r	0.5240H
Magnetizing inductance	L_m	0.487H

Table 4.1: Motor data used in simulation to show expected steady state performance of lab motor. The motor data were sampled from various sources to be similiar to that of the Terco lab motor, but mostly from table 5.1,[7] [13]

2.2 and 2.3 as well as lectures from Gonzalo Abad Biain on Youtube [14]. The system was developed for a generator rated 2MW, but the core concepts are the same where the main regulatory components are PI regulators controlling the DC-bus voltage, torque and speed and the dq components of the current. The simulation does not include a proper start-up procedure you would go through when doing experiments in real life, but the simulation goes to the steady state values after a few seconds. Table 4.2 shows the motor data that was used in the simulation. Figure 4.1 shows the overview of the main components in the simulation. The rotor and grid side controller contains state vector transformations and PI regulators for the dq-components of the currents.

The control loops are shown in figure 4.2. Figure 4.3 shows the torque coefficient as a function of tip speed and the power curve as a function of wind speed in meters per second.

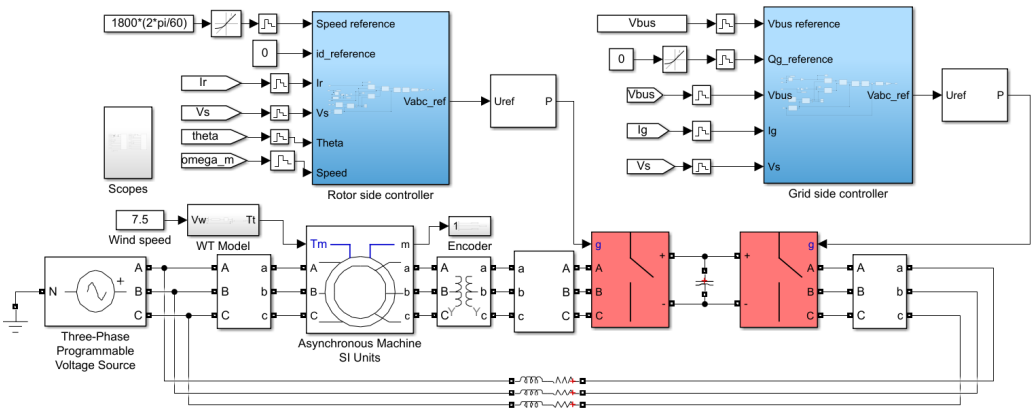

Figure 4.1: Simulation in Simulink of DFIG with rotor and grid side controller.

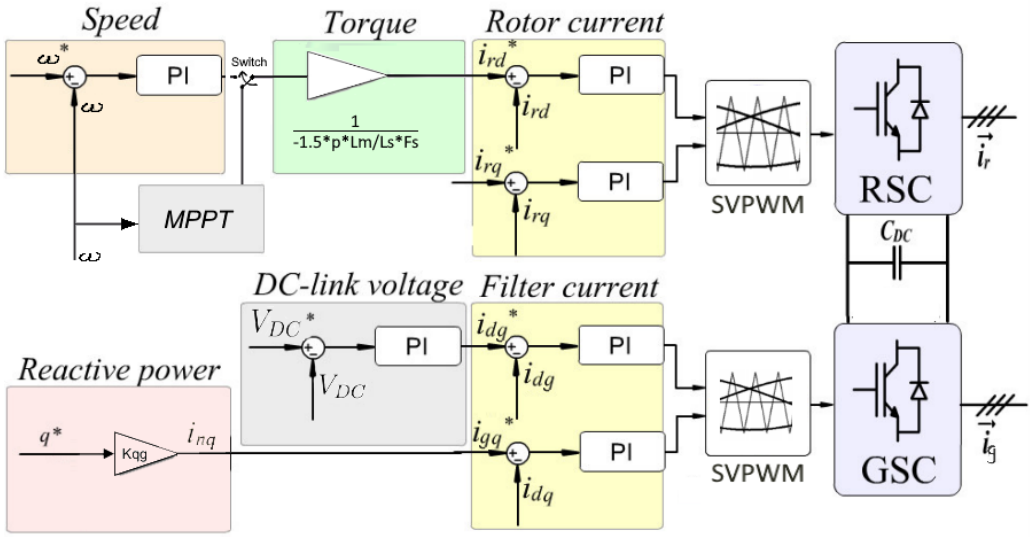

Figure 4.2: Control loops in the rotor and grid side controller. Adapted from [15]

General Motor and Converter Data 2MW		
Power	P_{mec}	2MW
Stator voltage	V_s	690V
Stator current	I_s	1760A
Rotor voltage	V_r	2070V
Rated speed	ω_m	1500rpm
Rated torque	T_{em}	12632Nm
Pole Pairs	P_P	2
Stator rotor turn ratio	u	3
Stator resistance	R_s	2.6mΩ
Stator and rotor inductance	L_s and L_r	2.6mH
Magnetizing inductance	L_m	2.5mH
Intertia	J	$127kg/m^3$
Dampening	D	1mNms
Filter resistance	R_g	20$\mu\Omega$
Filter inductance	L_g	400μH
DC-Bus capacitance	C_{bus}	80mH
DC-Bus voltage	V_{bus}	1150V

mondragonunibertsitateaDFIMTutorialImplementation2017

Table 4.2: Motor data used in simulations to show control systems response to torque changes.

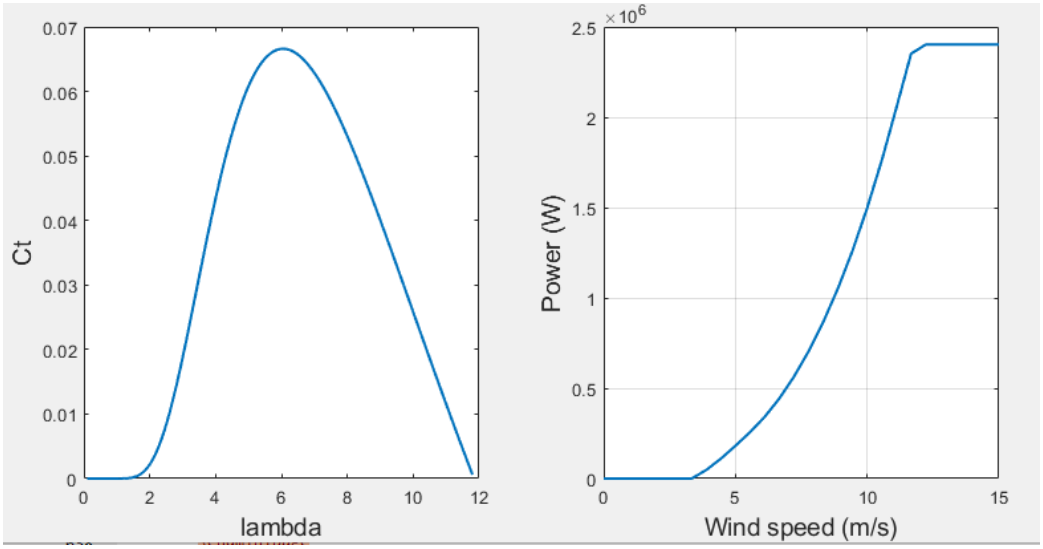

Figure 4.3: Torque coefficient and power curve for simulation of 2MW wind turbine. [16]

4.3 Embedded Coder with Matlab and Simulink

To make the simulation program into code, which is useable in a laboratory setting, an embedded coder function in Simulink is used. The embedded coder integrates the Delphino Launchpad and generates C-code for Code Composer Studio from the Simulink program. This also makes it possible to create blocks in Simulink which corresponds directly to the different pins on the controller, which makes programming significantly easier as it requires no knowledge of the C programming language. From testing the embedded coder, not every function transfer well to Code Composer Studios code. So it is possible some block might need to be substituted with an equivalent function.

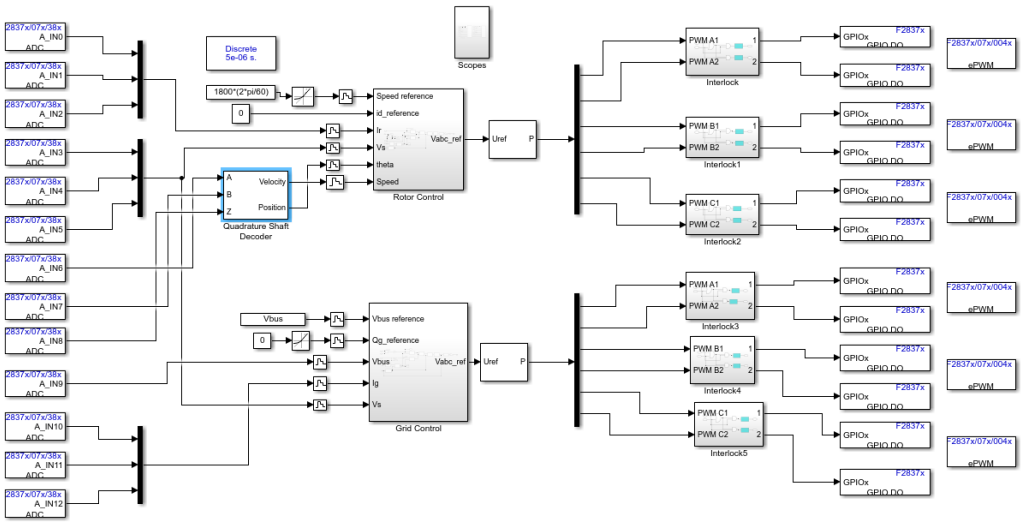

Figure 4.4: Simulink model to generate code with embedded coder for lab experiments where each box on the far side of the model is equivalent to a pin on the control card.

Chapter 5

DFIG Laboratory Model

The laboratory model is being developed at the power electronics laboratory at HVL and a block diagram of the whole model is shown in figure 5.1. The motor is from Terco and is a lab style motor with banana plug connectors for the stator and rotor windings. The rotor is connected through two converters controlled by the C2000 Delfino Multi Controller Unit (MCU) and the MCU samples currents and voltages through voltage and current transducers. The motor is powered through a 400/230V transformer.

5.1 Doubly Fed Induction Generator

The generator used in the HVL laboratory for this assignment is the Terco MV1007-405 induction motor with slip rings connected to the rotor. The characteristics and data of the electrical machines from Terco are similar to those of larger machines. Table 5.1 shows the general motor data provided by TERCO[17]. Figure 5.2 shows the motor located at the HVL-lab which will be connected to a motor with variable speed and torque to simulate a wind turbine. It will also be outfitted with an optical encoder to read the position of the rotor.

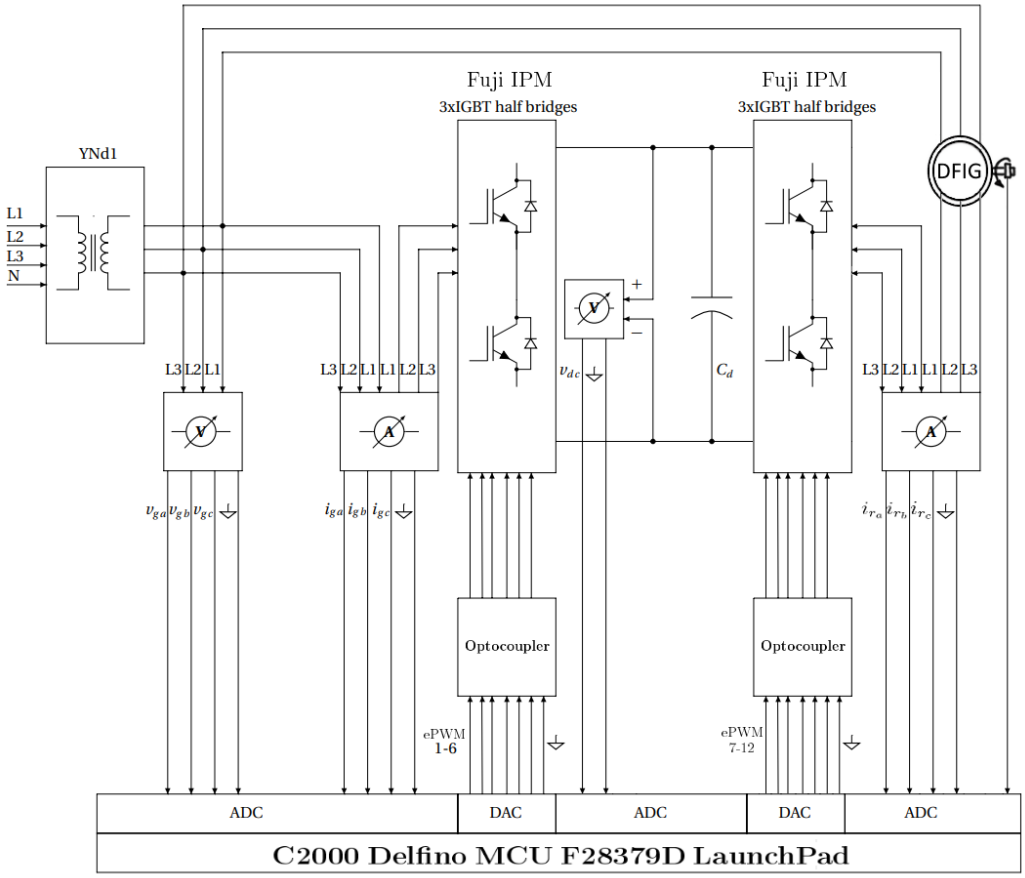

Figure 5.1: Block diagram of the laboratory model. Adapted from [9]

General Data	50Hz	60Hz
Power	1.1kW	1.1kW
Speed	1440rpm	1680rpm
Star Connection	380-415V, 3.2A	380-415 V, 3,2 A
Delta Connection	220-240V, 5.5A	220-240V, 5.5A
Secondary	260V, 3.0A	260V, 3.0A
Moment of intertia	$0.012 kgm^2$ (approx.)	

Table 5.1: General data for Terco MV1007-405 provided in the motor datasheet.

Figure 5.2: Picture of the TERCO MV1007-405 slip ring induction motor.

5.2 Incremental Optical Encoder

Knowing the rotor position and speed is required for the control system as covered in section 2.3.2. The encoder has three main signal types often called A, B and Z. A and B are offset from eachother and tells the control system if the rotor is moving, and Z gives one pulse for every full rotation. The incremental encoder will be mounted to the rotor of the motor and connected to the converter PCB for power and connection to the control card. In figure 5.1 you see the incremental encoder on the right side of the DFIG. The encoder used is shown in figure 5.3. [18]

Figure 5.3: Picture of Kübler incremental optical encoder.

5.3 C2000 Delfino MCU F28379D LaunchPad™ development kit

For controlling the DFIG converters, a development board from Texas Instruments is used. This board is a cheap option for general lab assignments that require something more powerful than boards like the Arduino Uno. The price is in the $\sim$ 40$ range, which makes it ideal for small scale power electronics projects. The board has both female and male pin headers which makes it suitable for stacking PCBs together or separately through jumper wires. The board can be connected through USB-2, where it communicates using a free program from Texas Instruments called Code Composer Studio. The board can also be integrated with MathWorks programs such as Simulink, where you can generate code for Code Composer Studio from the Simulink model. [19]

The board can sample analog signals through the ADC (analog-to-digital) ports which is ideal for measurements that are used in the control strategies explained in chapter 2.3. The maximum values the card can sample without being damaged is between -0,3V and 4,6V. This means that the signal the card samples from needs to be scaled to be between these values. [10]

The pulse width modulators on the board act as complementary pairs to ensure the correct management of the high- and low-side switches of one leg. The ePWM module has several features including a built-in dead time feature to prevent the top and bottom IGBT to turn on at the same time.

For rotor position and speed the board also has two Quadrature Encoder Position interfaces (eQEP). The eQEP ports are located at the bottom of the board as seen on figure 5.5. If required, the board supports absolute position encoders where both eQEPs are used at the same time. For this assignment however an incremental encoder is used which only requires one eQEP. [20]

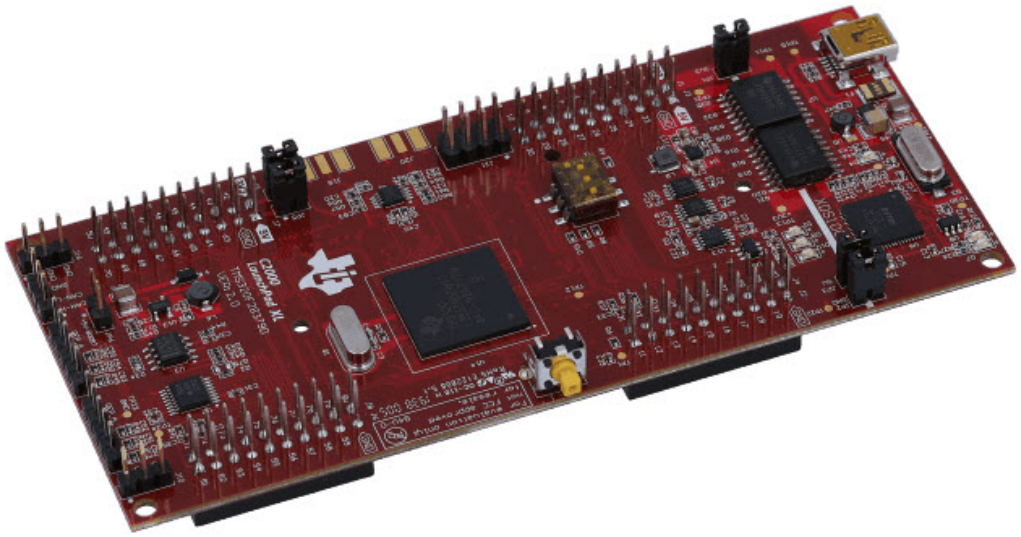

Figure 5.4: Picture of C2000 Delfino LaunchPad

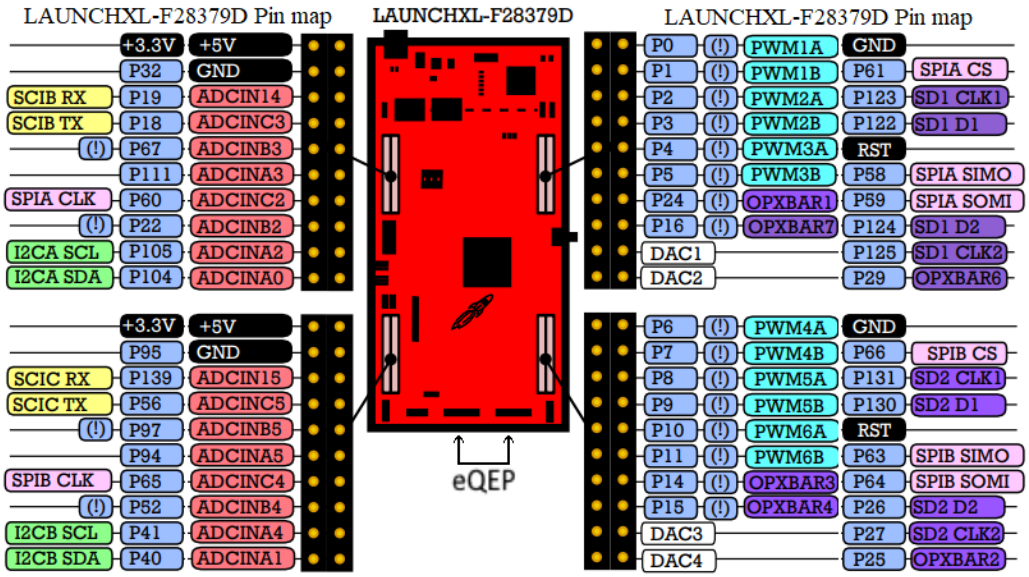

Figure 5.5: Picture of C2000 Delfino LaunchPad Pins. Adapted from [21]

Chapter 6

DFIG Converter Design

The circuit boards for the DFIG converter designed for this assignment were all done through EasyEDA which is an online PCB design tool. The website can be used to draw both schematics and PCB design. It also incorporates the schematic with the PCB design seemlessyly which makes it suitable for small scale electronics projects.

Prior to this assignment I had no PCB design experience and each board had multiple iterations before the final prototype, therefore these boards are not something that would be useable commercially but rather for prototyping and demonstrating the core concepts of the assignment. The boards themselves are also significantly larger than they would need to be as making soldering the boards easier ended up being a goal in the later iterations of the boards. Therefore almost no surface mounted components were used because through hole components are significantly easier to solder by hand. For the same reason, the pads were also made bigger than needed to make heat transfer between the soldering iron and the pads easier.

6.1 Measurement and Scaling PCB

The different measurements circuits were sourced from Sagedal (2018) [9]. The circuits are designed to convert the signal it measures into a signal the control card can sample through its ADC ports. For this project, the voltage transducer LEM LV-25-P and the current transducer LEM LA-100-TP are

used which can handle voltages up to 500V and currents up to 100A. The transducers use the hall effect to measure and can be soldered onto the circuit board. [22] [23]

Because the ADC needs its input scaled to for example 0-4V, we use a scaling circuit similar to the one in figure 6.1 which allows transforming an alternating signal to something that wont damage the ADC ports.

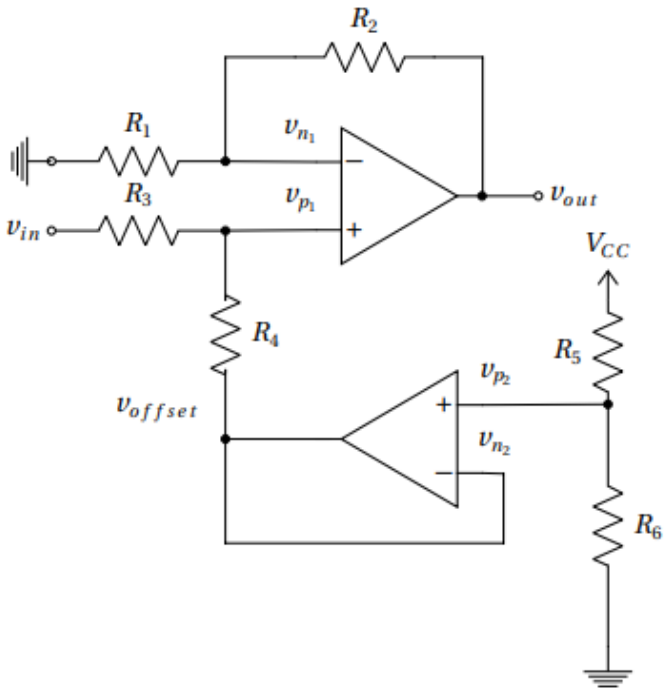

Figure 6.1: Scaling and offset circuit using operational amplifiers.

Assuming an ideal op amp with infinite amplification and infinite input resistance, we can use commonly known op amp theory to understand which resistors influences the output signal. For the bottom operational amplifier, we have

$$v_{offset} = V_{vcc}\frac{R_6}{R_5 + R_6} \tag{6.1}$$

And for the top operational amplifier we have in the v_{p1} node

$$\frac{v_{in} - v_{p1}}{R_3} + \frac{v_{offset} - v_{p1}}{R_4} = 0 \tag{6.2}$$

$$v_{n1} = v_{out}\frac{R_1}{R_2 + R_1} \tag{6.3}$$

Then combining equation 6.2 and 6.3 assuming $R_1 = R_3$ and $R_2 = R_4$ gives equation 6.4 which makes it easy to fit the output ADC signal to the output signal from the transducer and voltage divider.

$$v_{out} = \frac{v_{in}R_2 + v_{offset}R_1}{R_1} \tag{6.4}$$

6.1.1 Power supply

For both the measurement cards and the power modules we need +15V -15V and 0V supplied to the transducers and 15V to the IPMs and the optical rotor encoder. The voltage source is a power supply unit from the lab which is filtered through a ceramic and electrolytic capacitor on each board. We use the ceramic capacitor in parallel with the electrolytic capacitor because generally electrolytic capacitors are worse at filtering higher frequencies, this way we can filter out both high and low frequency noise.

6.1.2 Current measurement

To find the amplitude of the current we're measureing we know that the nominal power draw from the DFIG is 1.1kW and that the rotor power will be roughly one third of this. We can then calculate the peak current using Ohms law.

$$I_{p_n} = \frac{P_n \cdot \frac{1}{3}}{Vs} = \frac{1100 \cdot \frac{1}{3}}{230\sqrt{3}}\sqrt{2} = 1.3A \tag{6.5}$$

The primary and secondary circuit are galvanically separated with a winding turn ratio of 1:2000. The secondary current is then given by

$$I_{s_n} = I_{p_n}\frac{n_1}{n_2} = \frac{1,3}{2000} = 0,65mA \tag{6.6}$$

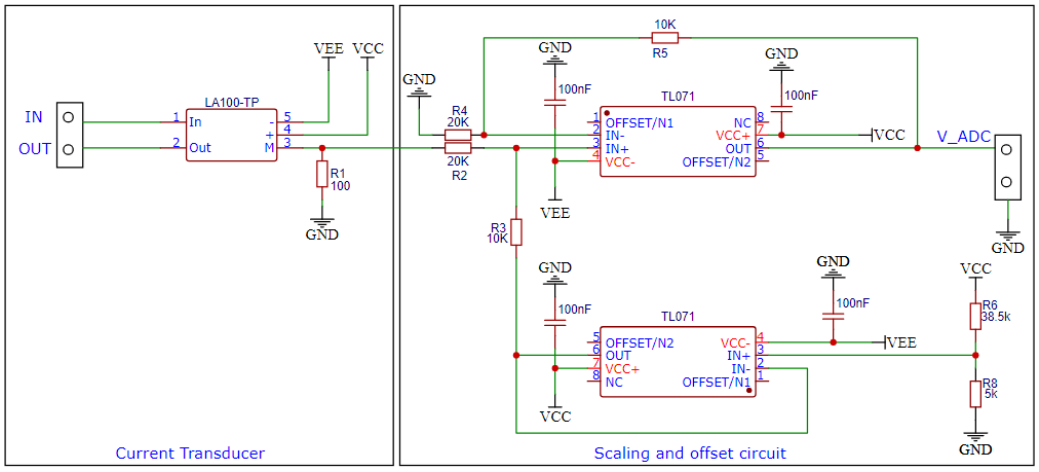

Figure 6.2: Current sensing circuit and scaling circuit.

The secondary side has a measuring resistor for thermal protection with a maximum value of 110Ω. Using a 100Ω resistor we get

$$v_{in} = I_{s_n} R_1 = \pm 0.00065 \cdot 100 = \pm 65mV \tag{6.7}$$

Then we can calculate the resistors of the scaling and offset circuit using the equations in section 6.1. First, we need to find which amplification to use

$$A = \frac{v_{out}}{v_{in}} = \frac{R_5}{R_4} = \frac{R_3}{R_2} = \frac{V_{ADC_{range}}}{v_{in_{range}}} = \frac{3,5V}{0,065V - (-0,065V)} \approx 27 \tag{6.8}$$

Knowing that the ratio between R_5 and R_4 is 1:27, one can set the resistors to 1kΩ and 27kΩ respectively. Using 6.8 we can also determine the scaling resistors and calculate the required v_{offset} using equation 6.4. v_{out} is 0V and v_{in} equal to -0,065V.

$$0 = \frac{-65mV \cdot 27k\Omega + V_{offset} \cdot 1k\Omega}{1k\Omega} \tag{6.9}$$

From this equation $v_{offset} = 1.755V$

Assuming that R_8 is 5kΩ and using the voltage divider formula we find R_6 equates to roughly a 38kΩ resistor.

6.1.3 Voltage measurement

The voltage circuit can be made using the same method as the current circuit.

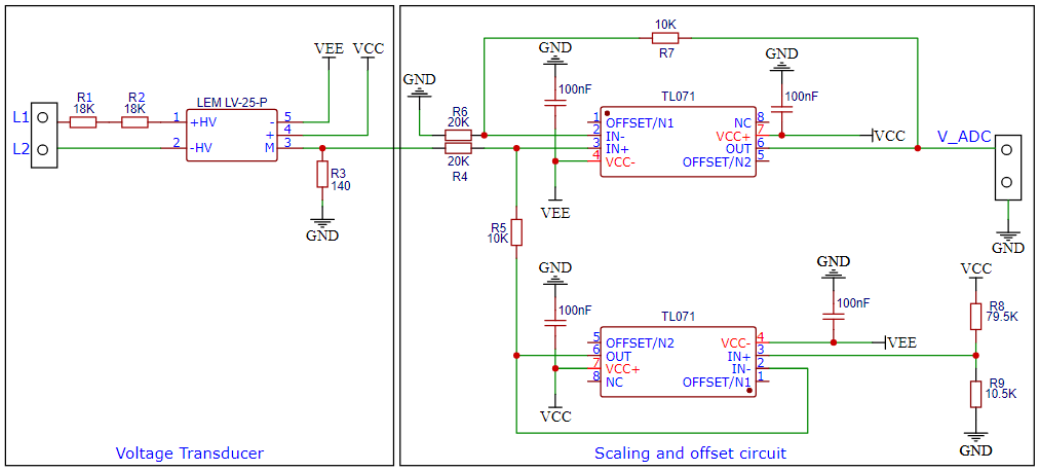

Figure 6.3: Voltage sensing circuit and scaling circuit.

At the primary side of the voltage transducer there will flow a current proportional to the potential difference. From the LEM LV-25-P datasheet we can see the nominal current is 10mA, so there needs to be an external resistance reducing the current. The nominal voltages measured are the line voltages v_{ab}, v_{ac} and v_{bc} and are assumed to be

$$V_n = 230\sqrt{2} = 325,27V \tag{6.10}$$

To leave some room for deviations from the norm, we set the voltage V_p to be slightly higher. The internal resistance of the transducer is measured to be 225Ω which is so low it can be neglected.

$$R_{eq} = \frac{V_p}{I_{p_n}} = \frac{360}{0,01} = 36k\Omega \tag{6.11}$$

Under maximum conditions the power dissipated over the external resistance will be

$$P_{R_1} = \frac{(\frac{V_p}{\sqrt{2}})^2}{R_1} = \frac{(\frac{180}{\sqrt{2}})^2}{18000} = 0,9W \tag{6.12}$$

Two resistors are used in the design, which halves the energy the resistors have to dissipate. Under 360V the current will be close to the nominal value, and with normal operating voltage the current will be equal to

$$I_{p_n} = \frac{V_p}{R_{external}} = \frac{325,27}{36000} = 9,04mA \tag{6.13}$$

From here we can use the same method as in the current measurement section. The thermal protection resistance is equal to

$$R_3 = \frac{\text{Maximum ADC input voltage}}{I_{s_n}} = \frac{3.5}{0.025} = 140\Omega \tag{6.14}$$

From here using 6.8 we get 0.5 amplication and assuming R_6 is 20kΩ we get R_7 equal to 10kΩ. Inserting these values into equation 6.4 we get

$$0 = \frac{-3.5V \cdot 10k\Omega + V_{offset} \cdot 20k\Omega}{20k\Omega} \tag{6.15}$$

From this equation we find $v_{offset} = 1,75V$.

Now calculating the voltage divider for v_offset assuming R_9 is 10.5kΩ we get R_8 equal to 79.5kΩ.

6.1.4 DC Voltage Measurements

The DC voltage measurement circuit uses the same LEM LV 25-P, but because the signal is constantly 3.5V with a measuring resistance of 140Ω, we do not need a scaling circuit before we connect it to the ADC on the control card.

6.1.5 Component layout

To limit the size of the circuit boards the rotor and stator measurement circuits were separated from each other. Therefore the circuit board needs to

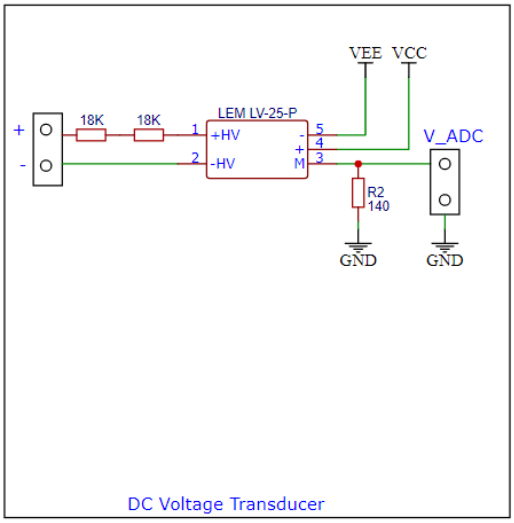

Figure 6.4: DC Voltage sensing and scaling circuit.

be connected by wires to the converter board. The wires between the cards are terminated using a pluggable terminal block from Phoenix Contact with lever actuation. This allows for easy removal or connection of the different boards during prototyping.

Figure 6.6 shows the rotor measurement circuits. Because this board only has three transducers compared to six on the stator board, it is the smaller one of the two. The board has four layers where one of the inner layers is only used for ground. This partially to make routing the ground easier, but it also provides shielding to the scaling circuit.

The transducers are separated from the ground layer because the high voltage lanes are not sensitive to surrounding interference. Each phase is also separated from each other by a minimum distance according to the IPC-2221 standard. The minimum distances as a function of voltage can be seen in figure 6.5, where for peak voltage over $\sqrt{2}V_s = 325.3$ there should at least be 0.8mm spacing between the lines on external coated layers. Because this project is in its prototyping stage, we can afford to separate the lines well beyond this minimum distance as a safety precaution against short circuits.[24]

The lines themselves also need to have a minimum size for them to not get hot and degrade or ruin the PCB. Recommendations for the width of the

lines can also be found in IPC-2221 and is given by equation 6.16 and 6.17. These equations use the imperial unit mils which is a thousandth of an inch, but they can be converted to mm. First, we calculate the area:

$$Area[mils^2] = \left(\frac{I}{k(Temp\ Rise[^\circ C])^b}\right)^{\frac{1}{c}} = \left(\frac{1.3A}{0.048(10^\circ C)^{0.44}}\right)^{\frac{1}{0.725}} = \quad (6.16)$$

$$Area[mils^2] = 23.4$$

Where for external layers k = 0.048, b = 0.44 and c = 0.725 and the current is 1.3A. Temperature rise is how many degrees above ambient temperature you allow. A safe limit for most PCB material is about 10°C. Then we can calculate the width using equation 6.17.

$$Width[mils] = \frac{Area[mils^2]}{Thickness[Oz] \cdot 1.378[mils/oz]} \quad (6.17)$$

$$Width[mils] = \frac{23.4}{1[oz/ft] \cdot 1.378[mils/oz]} = 16.98mils \approx 0.431mm$$

0.431mm is significantly smaller than the space available on the board, therefor there is no issue related to the current carrying lines getting hot with the current load. The thinnest part of the phase lines is $\approx 2mm$ on the IGBT card which equals a maximum rating of about 4A.

Vpeak (V)	Internal (mm)	External, uncoated (mm)	External, coated (mm)
15	0.05	0.1	0.05
30	0.05	0.1	0.05
50	0.1	0.6	0.13
100	0.1	0.6	0.13
150	0.2	0.6	0.4
170	0.2	1.25	0.4
250	0.2	1.25	0.4
300	0.2	1.25	0.4
500	0.25	2.5	0.8
> 500	0.25 + (V-500) × 0.0025	2.5 + (V-500) × 0.005	0.8 + (V-500) × 0.00306

Figure 6.5: IPC-2221 conductor spacing requirements.[24]

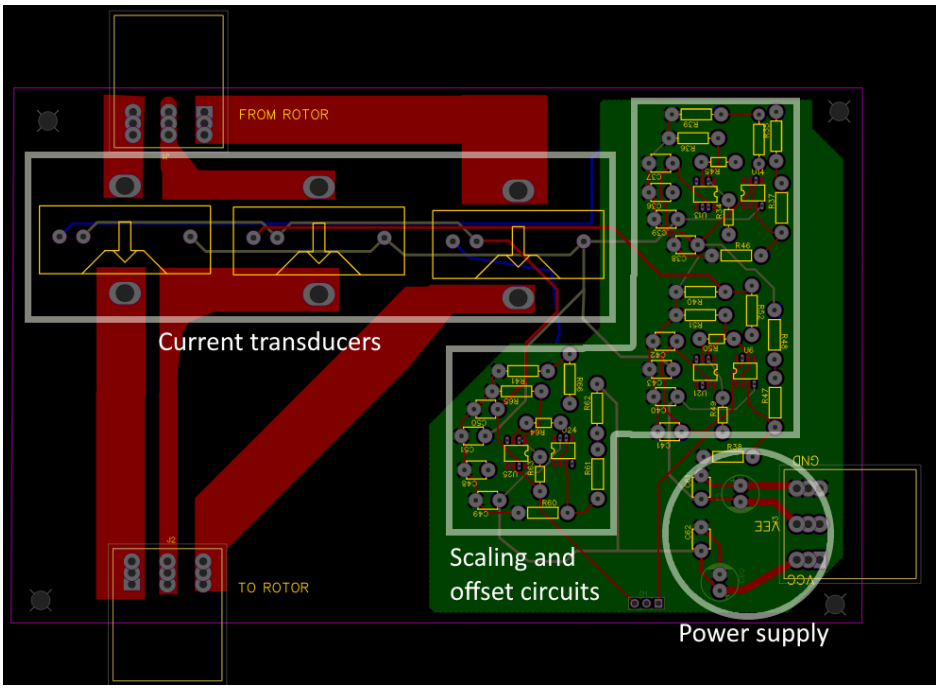

Figure 6.6: Circuitboard design for rotor current measurements

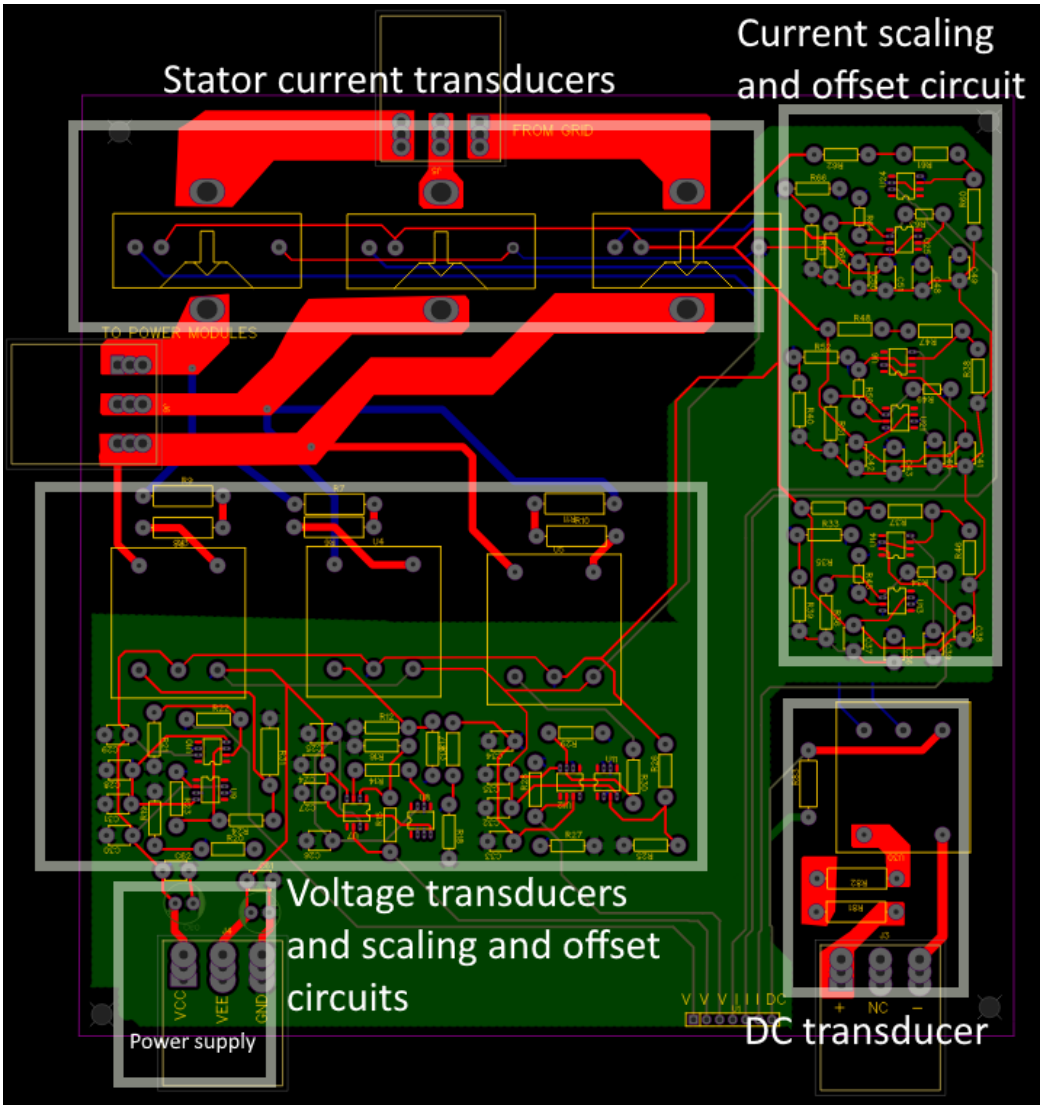

Figure 6.7: Circuitboard design for stator current and voltage measurements

6.2 IGBT Converter PCB

The converter PCB contains two Fuji Intelligent Power Modules (IPM) with a DC-link that has space for three bulk capacitors to smooth the DC output. It also has a slot for the control card and connectors for signals to the control card ADC and the optical shaft encoder. The schematic of the PCB is shown in figure 6.8.

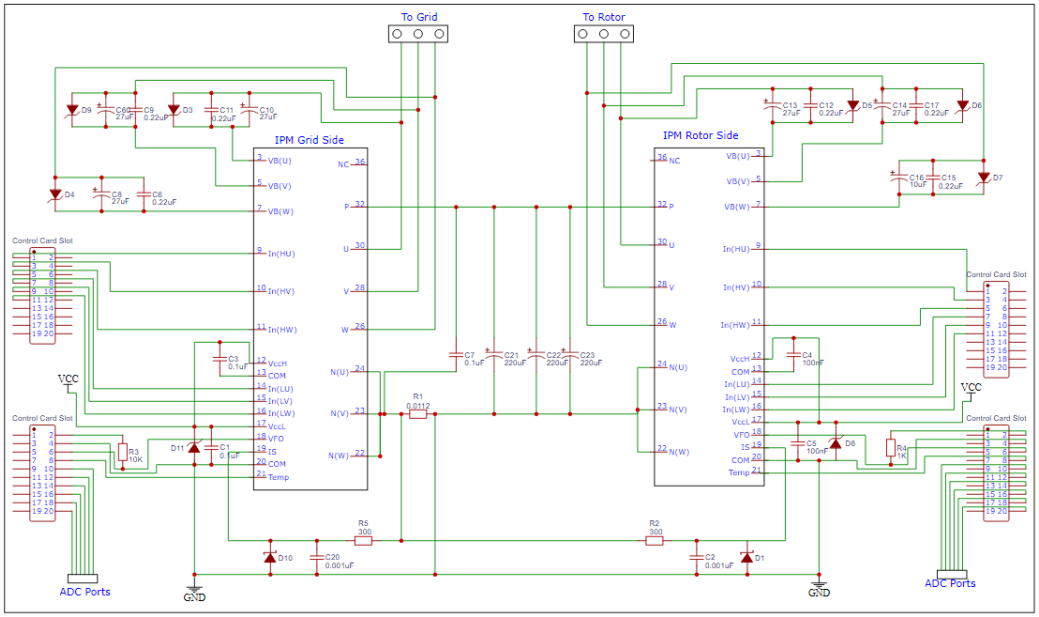

Figure 6.8: DFIG converter schematic showing the two Fuji IPMs, the control card slots and the components on the board.

6.2.1 Fuji IPM

Fuji Electric has designed the IPM used in this project. It is a small capacity IGBT drive circuit which is ideal for general motor drive applications. The model number is 6MBP15XSF-060-50 and is rated for 600V 15A. Figure 6.9 shows the ports on the IPM, where the right side is the high voltage side and the left side is everything related the control and safety features. The six IN ports are the gate drive signals which is fed by the PWM generator on the control card, and the V_{CCL} and V_{CCH} ports are fed by the 15V power supply.

The module also has two safety features which can detect too high current

through the converter and too high temperature. It can output a fault signal to the control card making it part of the overall control system. The one notable security feature this module does not have is an internal dead time between the upper and lower IGBT switching on/off. The recommended value in the datasheet is 1μs, which needs to either be implemented through an external circuit or through software in the control system. [25] [26]

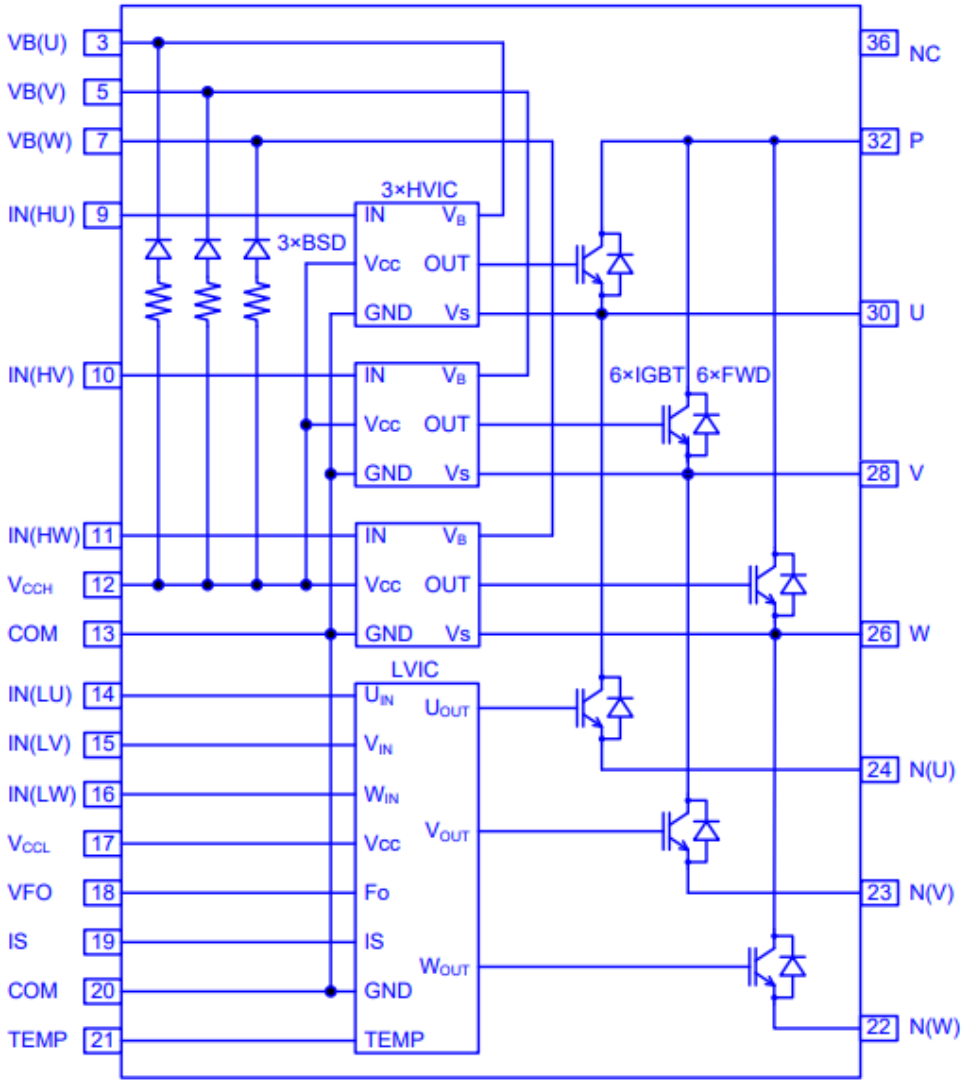

Figure 6.9: Internal circuit in Fuji IPM. [26]

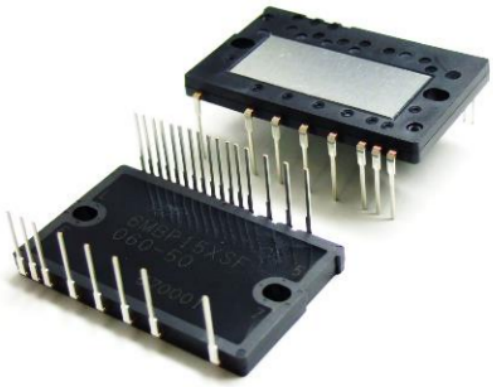

Figure 6.10: Picture of Fuji IPM[26]

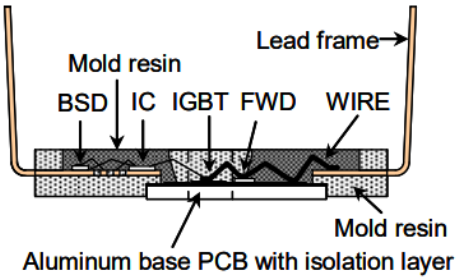

Figure 6.11: Cross section of Fuji IPM [26]

6.2.2 DC Bus

The DC bus shown in figure 2.8 between the two IPMs has slots for three through hole capacitors rated for 450V max and 220μF on the PCB. The main goal of the DC bus is to maintain a smooth DC voltage which does not affect the overall performance of the control system. To find the ripple voltage we have equation6.18 - 6.19. [27]

$$i_c = C\frac{dv}{dt} \tag{6.18}$$

Rearranging the equation we get

$$C = \frac{i_c \Delta t}{\Delta V} \Rightarrow V_{pp} = \frac{i_c}{f_{sw} C} \tag{6.19}$$

To find out if 660μF is enough I created a small simulation in Simulink using a $\approx$ 350W load fed by a three-phase diode rectifier to check the ripple of the voltage across the load. This model is a rough representation of the DFIG converter's DC-bus and the results can be seen in figure 6.12 and 6.13. From equation 6.19 we know that with increased switching frequency the ripple becomes smaller, and in figure 6.12 we can see that the ripple V_{pp} is 4V. With a switching frequency closer to 20kHz, one can expect significantly smaller

ripple voltage, therefore a capacitor size of 660μF is more than adequate for this DC link.

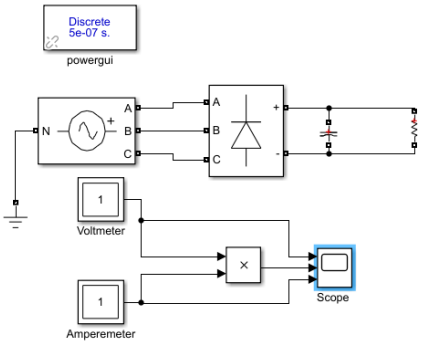

Figure 6.12: Simulink model

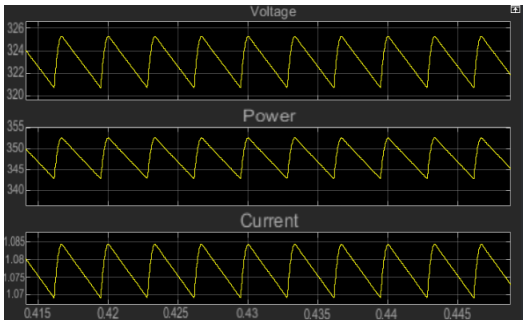

Figure 6.13: Voltage power and current ripple with 660μF capacitor.

6.2.3 Bootstrap Circuit to Power Upper IGBTs

A bootstrap circuit shown in 6.14 is a method of supplying power to the high side gate drive circuitry in the IPM. The circuit is comprised of a bootstrap diode, a bulk capacitor, a filter capacitor and a zener diode for overvoltage protection. The bulk capacitor is a larger electrolytic capacitor designed to hold the energy of the gate terminal, while the filter capacitor is a smaller ceramic one. [26]

When choosing a bulk capacitor, we need to consider a few properties such as voltage ripple and the turn on time for the transistors. From the datasheet we find that the average circuit current of the bootstrap circuit is about 0.2mA when charging the capacitor with 15V.

Assuming a duty cycle of 90%, the maximum on pulse width is given by

$$t_1 = \frac{1}{f_{sw}} D = \frac{1}{20000} 0.9 = 45\mu s \tag{6.20}$$

There is no recommendation for a minimum ripple voltage from Fuji. We assume a maximum dV = 1 mV for the rest of the calculations. The parameters of the capacitor is given by equation 6.21.

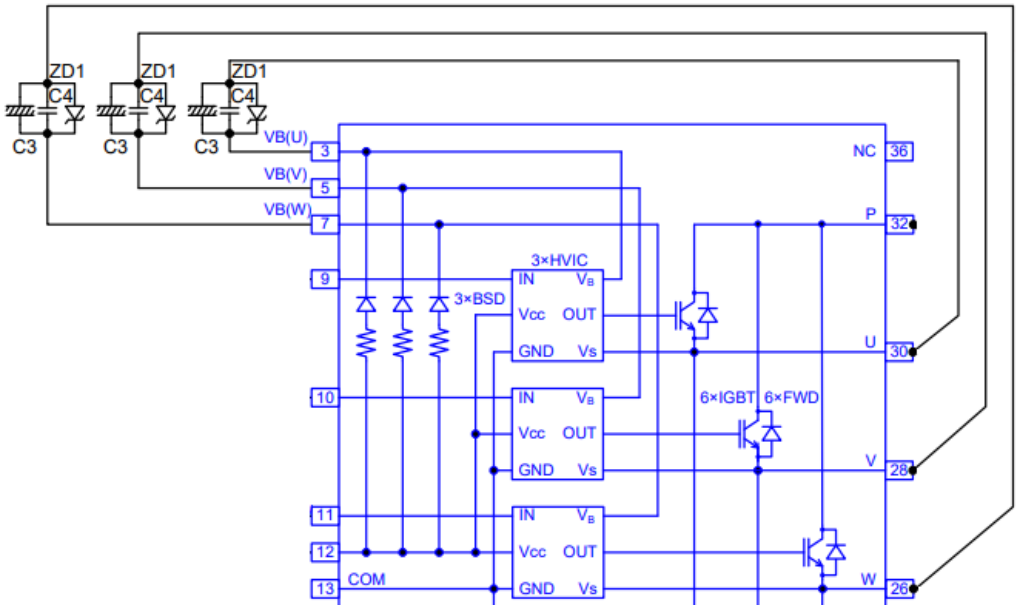

Figure 6.14: Bootstrap capacitor circuit at the top of the Fuji IPM.

$$C = I_b \cdot \frac{t_1}{dV} = 0.2mA \cdot \frac{45\mu s}{1mV} = 9\mu F \tag{6.21}$$

Fuji recommends a safety margin of 2-3 times the capacity so we get 27μF capacity:

$$C_b = C \cdot 3 = 9\mu F \cdot 3 = 27\mu F \tag{6.22}$$

When starting the IPM the bootstrap capacitors need to be charged by turning on the lower transistors. This is done by turning on pin 14, 15 and 16 until the capacitor is charged. The charging time will be equal to five times the time constant τ of the bootstrap circuit. From the IPM manual it says "For reference, the charging time of a 10μF capacitor through the internal bootstrap diode is about 2ms." From this we get a rough estimate of what 5τ is.

$$\tau = C \cdot R \Rightarrow R = \frac{\tau}{C} \tag{6.23}$$

$$R = \frac{2ms}{10\mu F} = 200\Omega \tag{6.24}$$

$$\tau_{27\mu F} = 27\mu F \cdot 200\Omega = 5.4ms \tag{6.25}$$

The minimum pulse width is also noteworthy and is decided by the minimum on pulse width of the lower side IGBT or the minimum off pulse width of the upper side IGBT, whichever is smaller. The minimum pulse width is given by equation 6.26.

$$t_2 \leq \frac{R \cdot C \cdot dV}{V_{CC} - V_{b(min)}} \tag{6.26}$$

- R: Series resistance of boostrap diode.
- C: Boostrap capacitance
- dV: the allowable discharge voltage
- V_{CC}: Voltage of HVICs and LVIC power supply
- $V_{b(min)}$: the minimum voltage of the upper side IGBT drive

To find the BSD resistance we have to consider figure 3-14 in the Fuji IPM application manual. Figure 6.15 shows the characteristic of the BSD (Bootstrap Diode) resistance. At 15V forward voltage we get roughly 7Ω through the BSD. The maximum allowable discharge voltage is still 1mV and the bootstrap capacitance is 27μF. V_{CC} is 15V and $V_{b(min)}$ is 14V which gives [26]

$$t_2 \leq \frac{7\Omega \cdot 27 \cdot 10^{-6}F \cdot 0.001V}{15V - 14V} = 0.189\mu s \tag{6.27}$$

6.2.4 Stacked card slot

The PCB contains four female 10x2 pin headers whose purpose is to allow the control card to be stacked on top of the circuit board saving unnecessary wires between the cards. All the control card pins being connected to the converter PCB allows the signals from the optical encoder and measurement cards to

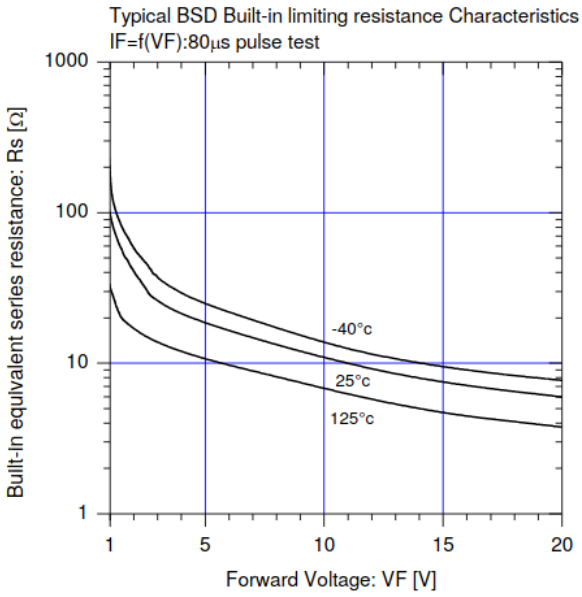

Figure 6.15: Equivalent series resistance of boot strap diode. [26]

be routed through the converter PCB. This has the advantage of cleaning up the amount of jumper cables required between various components and the control card. It also has the benefit of reducing noise sources for the PWM signals, as the distance between the card and the IGBT is smaller.

6.2.5 PWM Low Pass Filter

Noise can be a problem for PWM signals, so a low pass filter has been added on the PCB between the control card and the gate driver to reduce high frequency noise. For the low pass filter with 100Ω resistance and a 10nF capacitor we have a cutoff frequency of 159kHz from equation 6.28. The main reason for using a 10nF capacitor is the availability of capacitors at the lab, the cutoff frequency is not terribly important as long as it does not interfere with the PWM signal.

$$f_c = \frac{1}{2\pi RC} = \frac{1}{2\pi \cdot 100 \cdot 10 \cdot 10^{-9}} = 159kHz \tag{6.28}$$

6.2.6 Overcurrent Protection

The Fuji IPM has a built-in overcurrent protection using where a shunt resistor is used in the negative portion of the DC-link. [26]

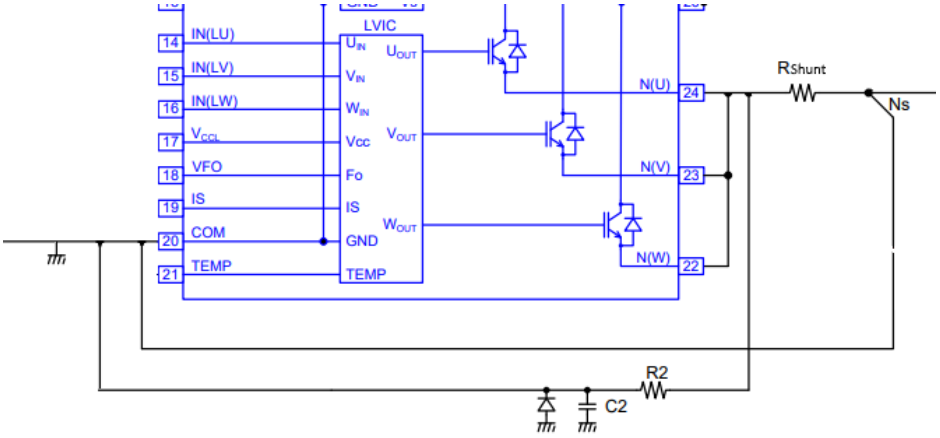

Figure 6.16: Fuji IPM overcurrent protection circuit using shunt resistor R_{shunt}

The shunt resistor is given by equation 6.29 and from the manual we have $V_{IS(ref)(max)} = 0.505$.

$$R_{Sh(min)} = \frac{V_{IS(ref)(max)}}{I_{OC}} = \frac{0.505}{45} = 11.2m\Omega \tag{6.29}$$

Between the shunt resistor and the Is terminal there is an RC filter to delay the voltage rise. The recommended delay is 1.5μs which is given by equation 6.30.

$$t_{delay} = -\tau \cdot ln\left(1 - \frac{V_{IS(ref)(max)}}{R_{Sh} \cdot I_p}\right) \tag{6.30}$$

Solving this equation for τ assuming the peak current flow through the shunt resistor is 45A we get $\tau \approx 0.3\mu s$. From this, assuming R2 = 300Ω, we get C2 equal to 0.001μF.

6.2.7 Optocoupler

The PWM output from the control card outputs 3.3V which is not enough for the IPM as the IPMs requires 15V. One solution is using optocouplers to boost the control signals up to 15V. An earlier project at HVL developed a PCB with six optocouplers for an inverter system. Using two spare PCBs from that project a simpler version using only the signal boosting part of the PCB was made. In figure 6.19 we can see the layout of the PCB, and only 6 of the integrated on the board are for the PWM signals, the rest are some signal for a different project not in use. The optocouplers also require a 15V signal in, which comes from the larger pads to the left. [28]

Figure 6.17 and 6.18 shows the circuit for a single converter leg and the internal circuit of the optocoupler CNY17F-3.

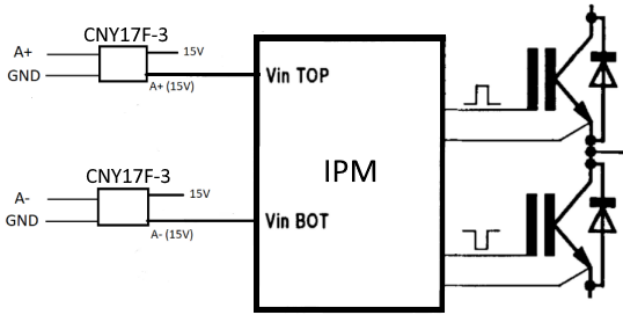

Figure 6.17: Optocoupler circuit.[28]

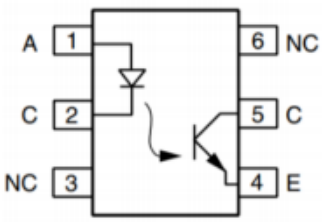

Figure 6.18: CNY17F-3

From the CNY17F-3 datasheet we have a maximum DC forward current of 60mA, therefore a ≈60Ω resistor needs to be in front of it. [29]

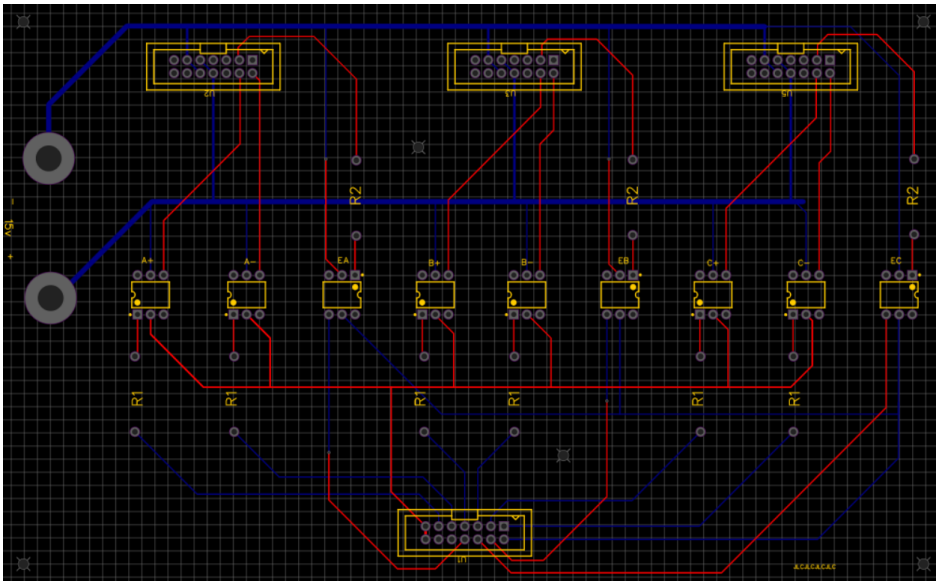

Figure 6.19: Circuitboard design for optocouplers to increase the voltage of the PWM signal to 15V.[28]

6.2.8 Component layout

The layout of the PCB can be seen in figure 6.20. There is also a grounding copper layer under the low voltage signals around the control card. Similarly, to the measurement cards, the high voltage part of the control card is separated from the low voltage signals. The same results from the calculations in equation 6.17 and 6.16 are used on this board to determine the minimum distance between the power lines. These widths and distances are oversized on the board because there is available space on the prototype card.

The bootstrap capacitors for the high side power supply are located as close to the terminals as possible to avoid potential influence of pattern inductances. There's also a zener diode in parallel with the capacitors to protect it from high voltage or negative voltage that can occur if the parasitic capacitance between VB(U,V,W) and ground is too high when the IGBT turns off and on with high dV/dt.

The measurement signal pins are placed close to the ADC pins of the control card. They are normal male pin headers which are connected to the measurement PCBs using jumper wires. The optical encoder ports are placed in a similar manner, except it is not for pin headers but for a small screw connector instead. This is so that optical encoder can be connected directly to the card.

The power supply is in the top right corner of the board. Because only positive 15V is needed on the board -15V is not present. Between the control slot card there are various filter capacitors and a 20V zener diode to prevent overvoltage.

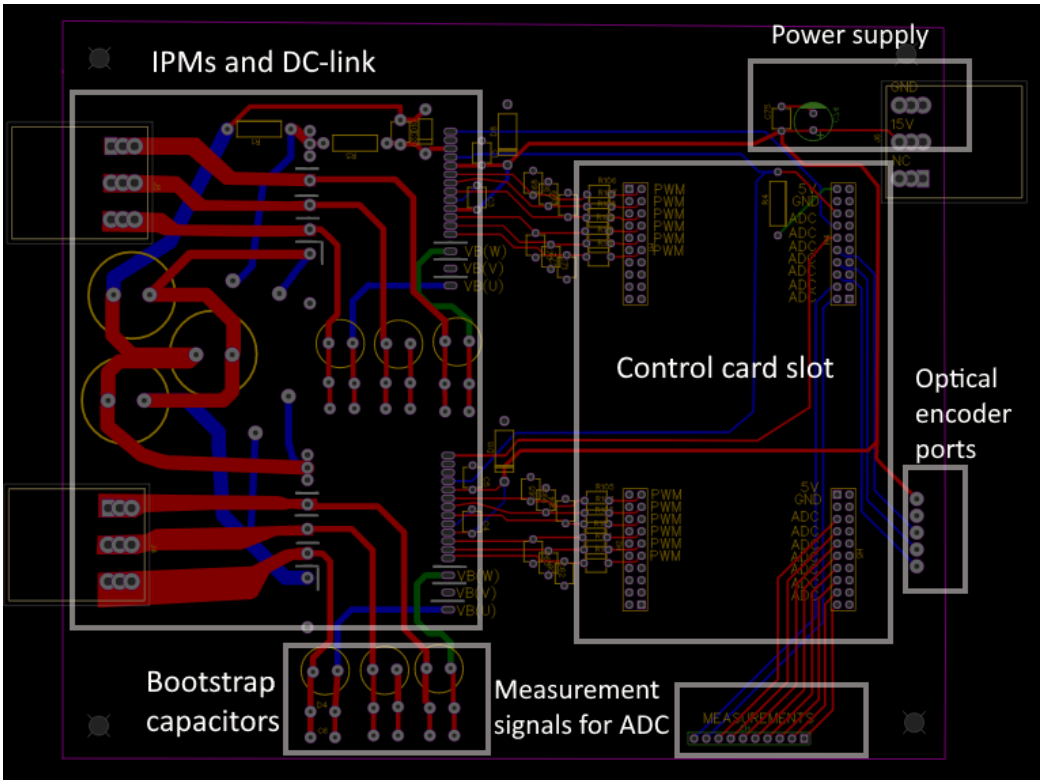

Figure 6.20: Circuitboard for IGBT converters designed in EasyEDA. Red lines are the top layer and the blue layer is the bottom layer. Green and yellow are inner layers. Under the control card there is also a hidden copper grounding layer for shielding.

Chapter 7

Results

The results of this thesis are the foundation for putting together a working prototype where one can conduct tests on a DFIG in a lab environment. The results are divided into three parts. 7.1 shows the result from the work in chapter 5 and shows prototype boards which while being untested, are a start for work on real hardware. 7.2 shows the expected steady state performance of the 1.1kW lab motor. 7.3 shows a simulated performance of the control system's response to torque changes on a DFIG.

7.1 Lab Model

The lab model has every board described in chapter 6 with most components soldered on. If there is components missing it is because of missing components. The figure descriptions includes a more detailed description of each board. The green contacts at the edge of the board is detachable from the board without removing the wires themselves which makes them ideal for prototyping.

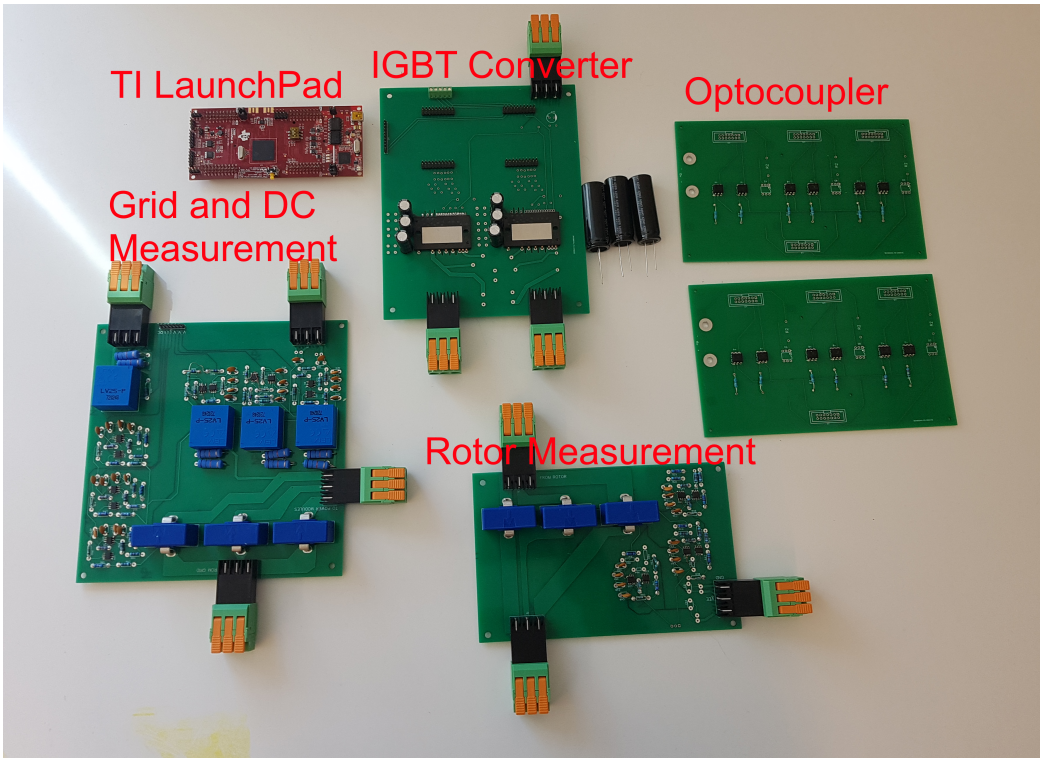

Figure 7.1: This is all the prototype PCBs together to show how big they are in comparison to each other. The most noteworthy thing is how big the measurement and scaling circuits are in comparison to the IPMs which are the two black squares on the top middle board. The measurement and scaling PCBs are the bottom middle one and the one to the left. The optocoupler PCB are to the right. The control card is the red one which would ideally be seated on the slot to the right of it.

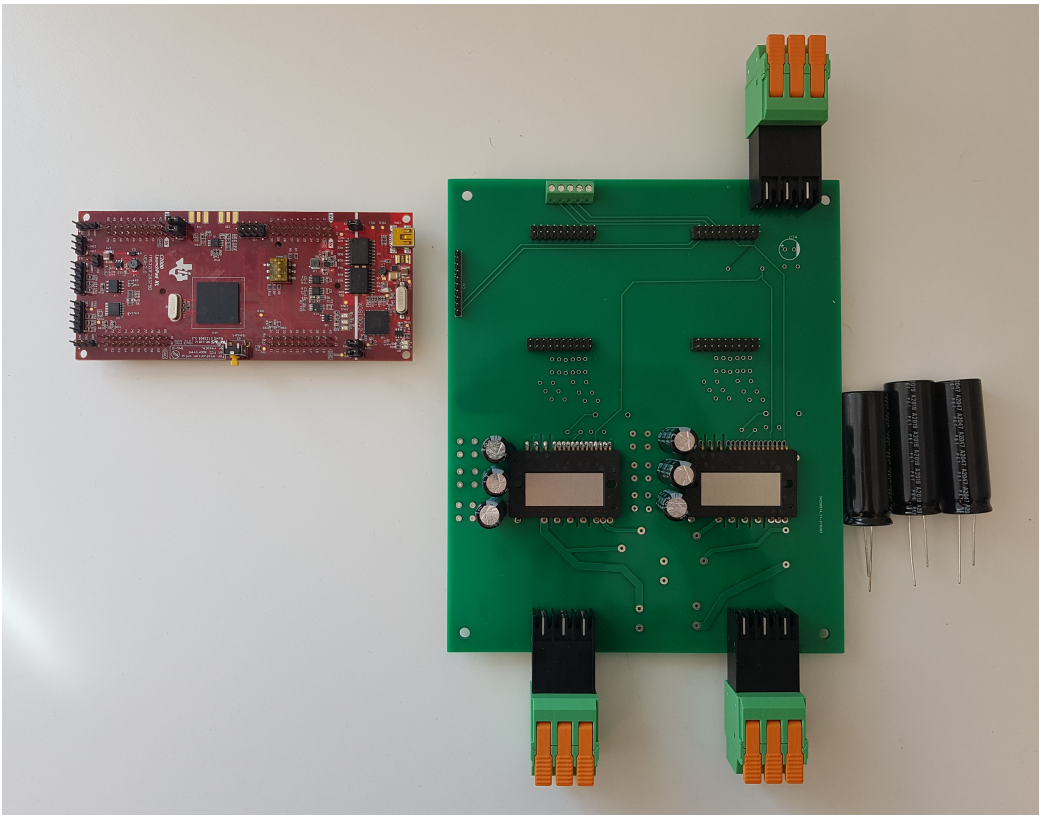

Figure 7.2: This is the converter PCB which is missing the most components. The top screw terminal is for the incremental optical encoder. The top right terminal is for the 15V power supply and ground. The capacitor on the right side is the bulk capacitors, and would be connected on the board in between the bottom two plug terminals. The small capacitors next to the IPMs are the bootstrap capacitors. The four black rectangles is the control card slot. The small black rectangle next to the control card on the left side are pin headers which is connected to the ADC ports of the control card slot. In between everything there is holes for various components which can be seen in more detail in figure 6.20 and 6.8.

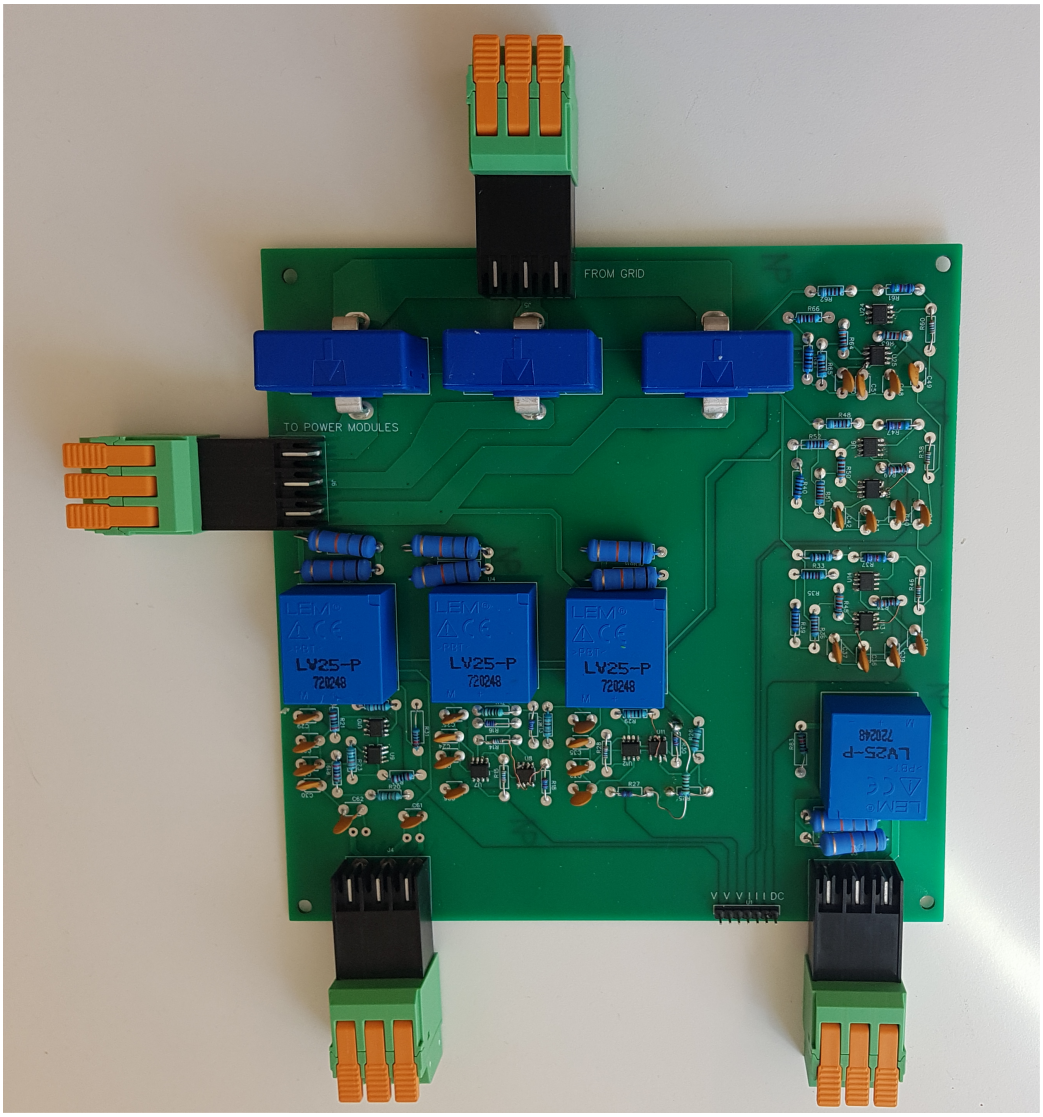

Figure 7.3: This is the PCB that measures and scales the grid voltage, DC voltage and the current going in to the converter. This is a mostly complete card, only component that is missing is the electrolytic capacitor at the power supply in the bottom left. The exact layout can be seen in more detail in figure 6.7.

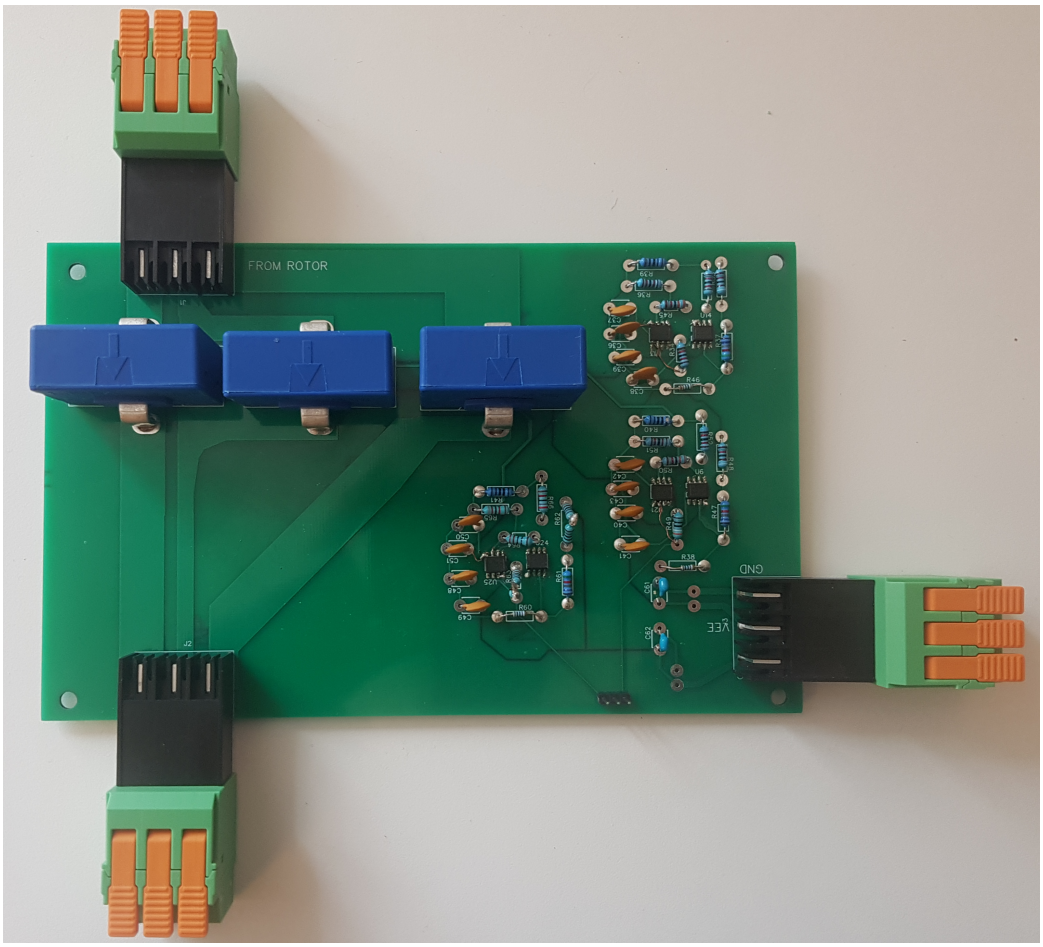

Figure 7.4: This is the PCB that measures and scales the rotor current. The board is mostly complete, although missing a few components. The exact layout can be seen in more detail in figure 6.6.

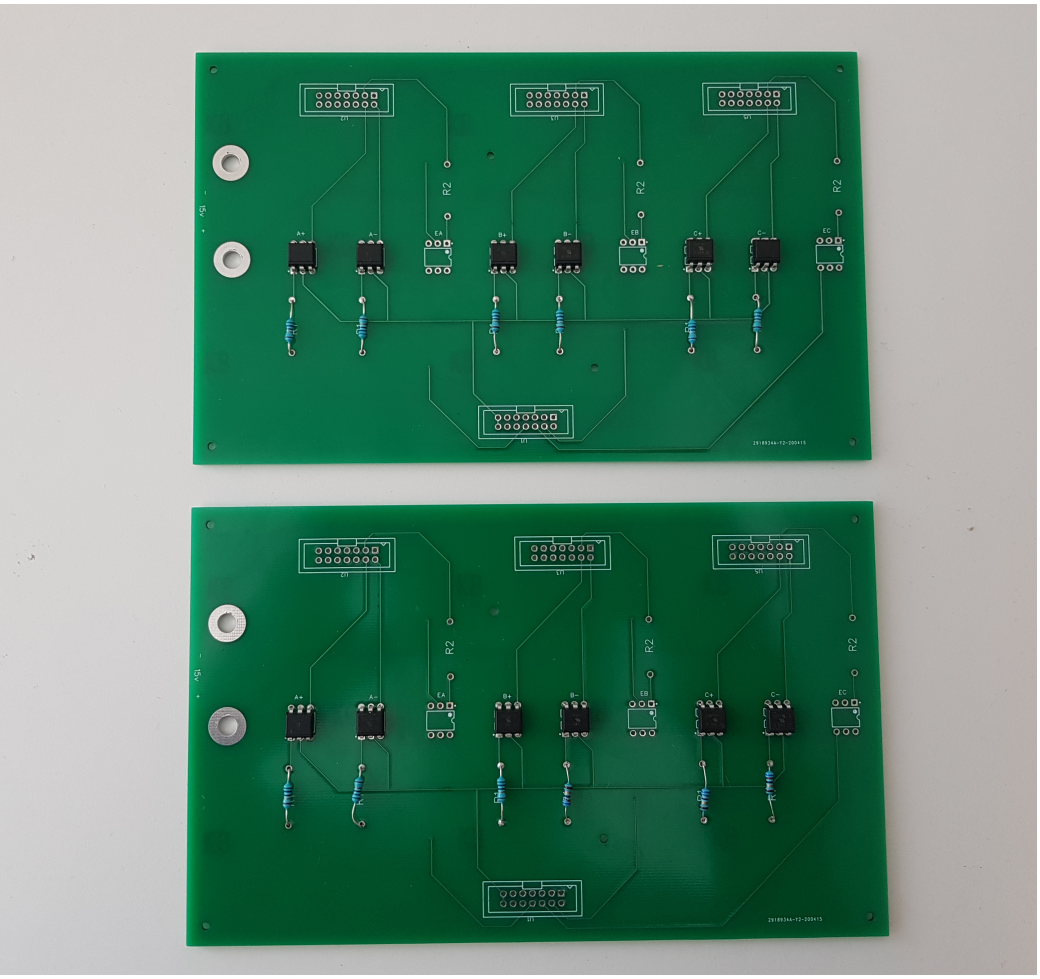

Figure 7.5: This is the optocouplers that is there to increase the voltage of the PWM signals. These PCBs are were spare from a previous thesis at the Western Norwegian University of Applied Science. Each chip on this board is for one PWM signal for a total of 12. The large pads on the left side of the PCB is for banana plug connectors with 15V.

7.2 Steady State Analysis of 1.1kW Lab DFIG

These figures shows the steady state performance of a 1.1kW motor similar to the one at the university lab. The red lines represent when the reactive stator power $Q_s = 0$, and the green lines represent when $i_{dr} = 0$

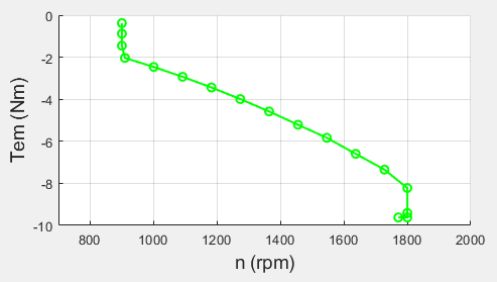

Figure 7.6: Torque as a function of rpm.

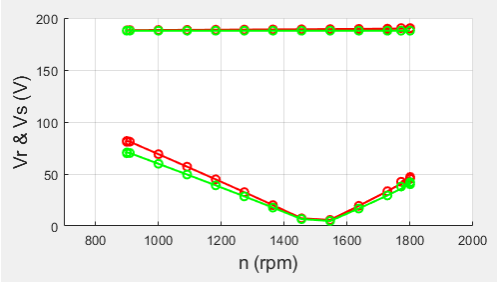

Figure 7.7: Stator and rotor voltage of DFIG.

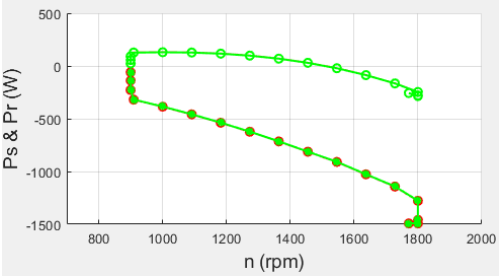

Figure 7.8: Stator and rotor power.

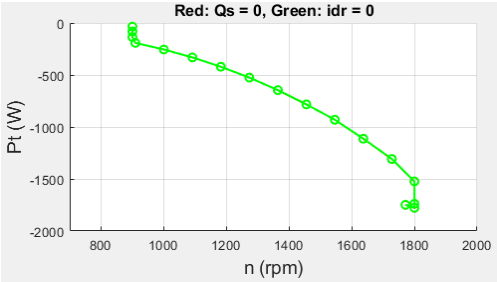

Figure 7.9: Total power delivered.

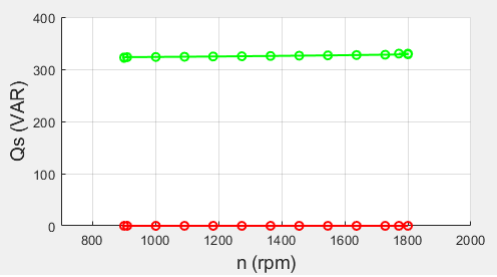

Figure 7.10: Reactive stator power.

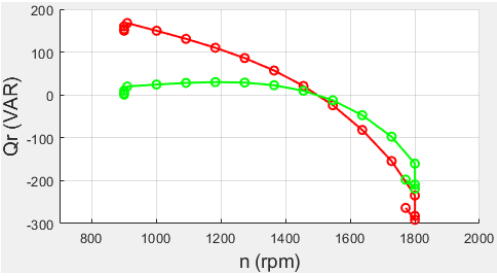

Figure 7.11: Reactive rotor power.

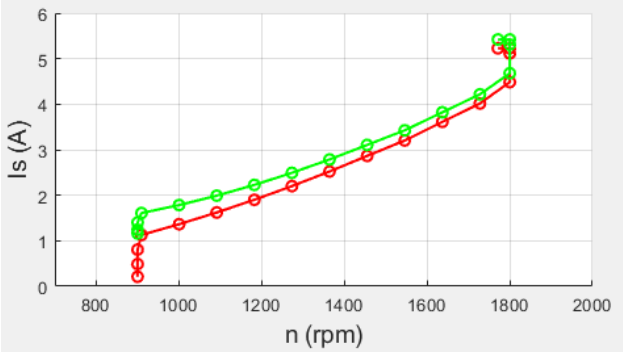

Figure 7.12: Steady state stator current of DFIG

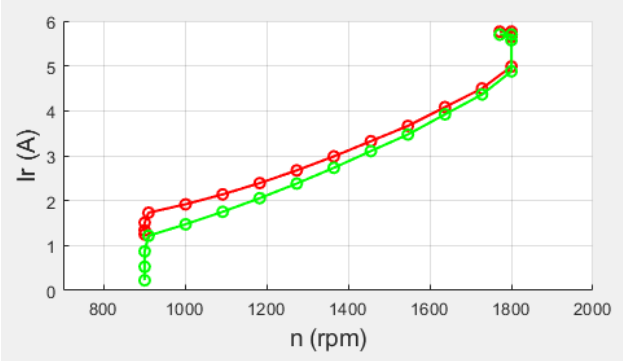

Figure 7.13: Steady state rotor current of DFIG

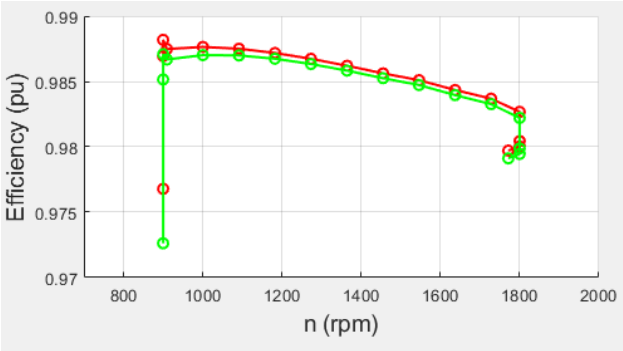

Figure 7.14: Efficiency of DFIG

7.3 Control System Response to Torque Changes

The results are a control system which can deal with rapid changes in torque from the wind turbine and circuit boards which can be used to test DFIG generators at the HVL lab. The control system simulation of a 2MW generator can be shown in figure 7.15 and 7.16, where the system manages to respond to torque changes and settles in a steady state after a short amount of time. The reference value is in the middle of the oscillation of the the measured value, and it is tracking the reference value as expected. This can be seen more easily in 7.16 where the reference value of the DC bus is 1150V and the control system is trying to approach that value. When the generator accelerates past DC current when DFIG is at synchronous speed one can see the current is not alternating in figure 7.17.

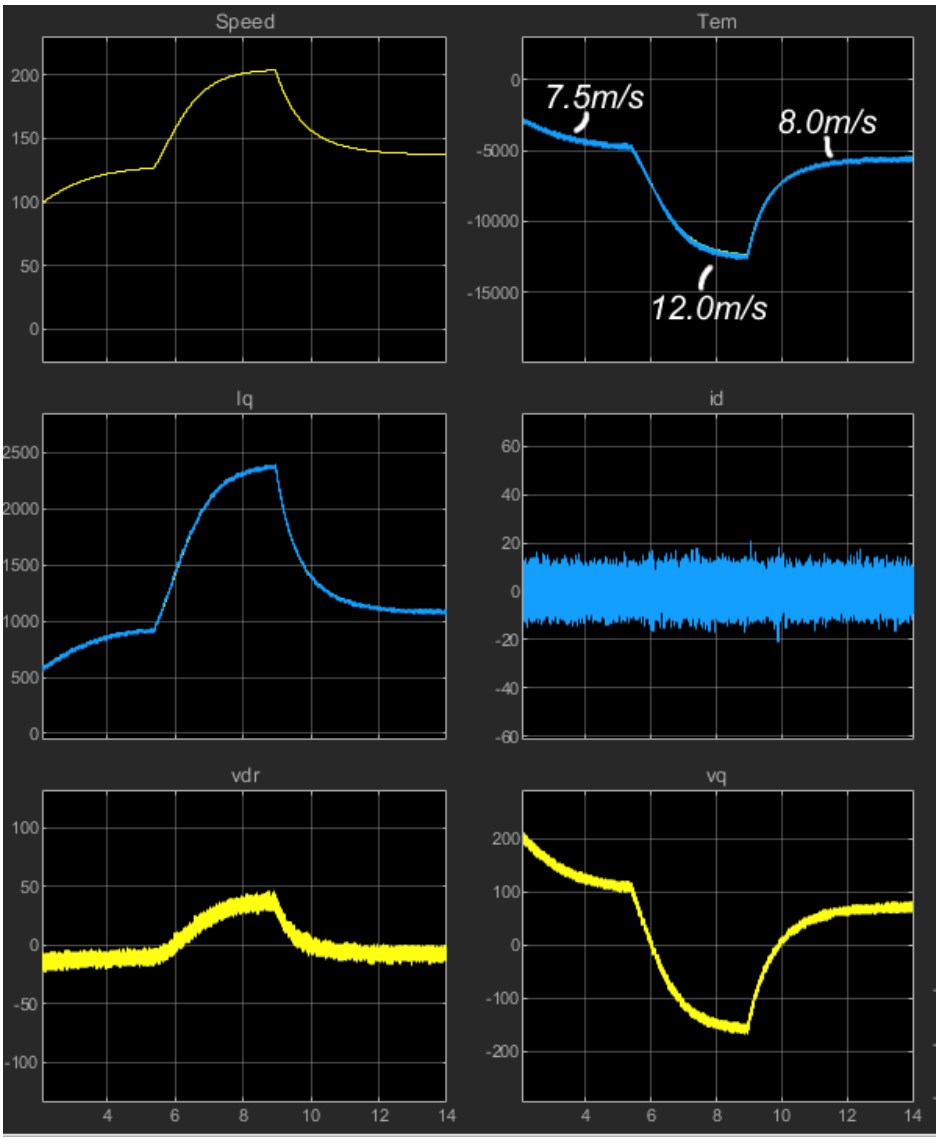

Figure 7.15: Rotor side control system response when the wind speed increases from 7.5m/s to 12m/s and back down to 8m/s. X-axis shows time in seconds

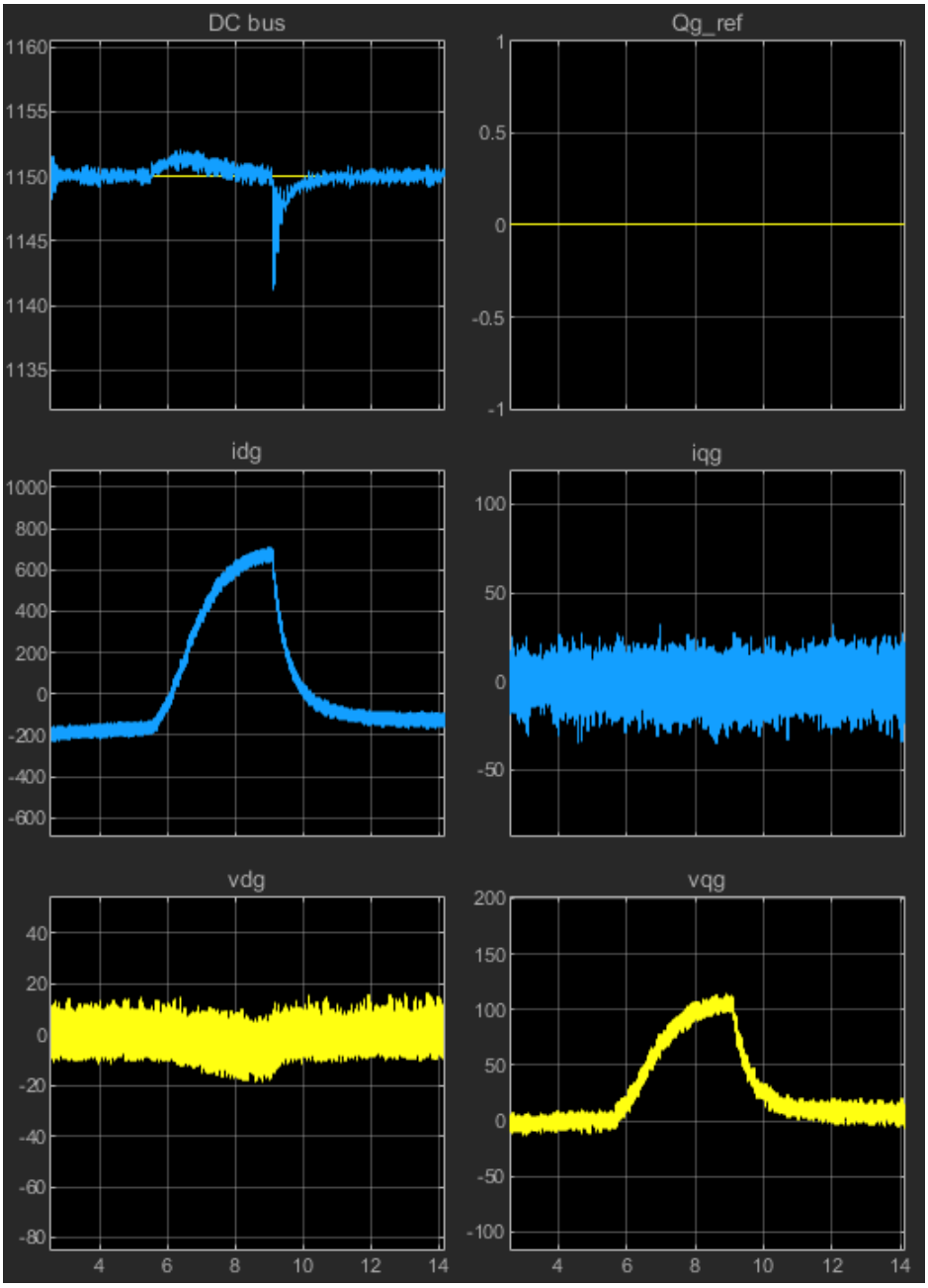

Figure 7.16: Grid side control system response when wind speed increases from 7.5m/s to 12m/s and back to to 8m/s. X-axis shows time in seconds.

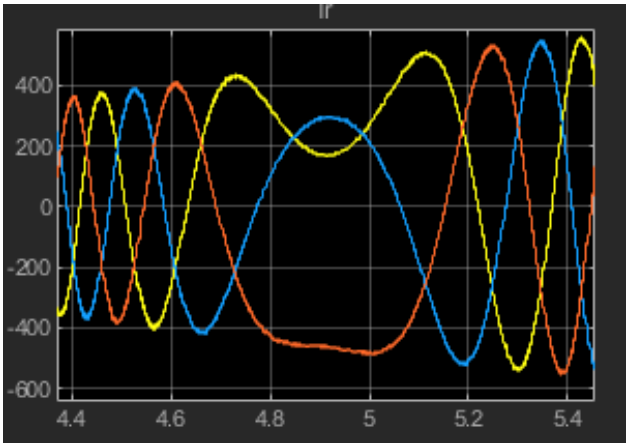

Figure 7.17: DC current when DFIG is accelerating past synchronous speed.

Chapter 8

Discussion

In this thesis the foundation for building a lab model of a DFIG has been shown, and components based on this foundation has been built. It has also been shown that you can create small scale DFIG converters using cheap compact IPMs. While the current hardware is in an early prototype stage, it could still be used to do experiments that confirms that the design works.

It also shows future potential for scaling the system down to something you could fit in a small container. This is because all the components in the current model is through hole components, and one could save a lot of space switching to surface mounted components. The main problem related to scaling down the system would be the current and voltage transducers. These components are relatively large in comparison to everything else and takes up a significant amount of surface area. If a different method which requires smaller components was used to measure and scale the currents and voltages, one could save quite a bit of space.

The PCBs themselves have not yet been verified that they work as intended, and it is possible that there are problems that needs to be fixed.

8.1 Controller and PWM Generation

On the IGBT converter PCB there is a slot for the controller which would eliminate the need for any jumper cables between the controller and the converter PCB. But because of a slight inaccuracy in the design, the slot

is slightly off from where it needs to be, and the controller does not fit. Therefore if one were to use the hardware produced in this thesis, one would have to add jumper cables between the controller slot and the controller. The optocouplers are also on its own board which would require cables.

When designing the converter PCB, a couple of useful control card features were overlooked. The control card has the ability to handle incremental encoders using the eQEP ports. But in chapter 4.3, the incremental decoder signals are sampled by the ADC ports and decoded by the quadrature shaft decoder block in Simulink. This would work but using the eQEP ports would be a better solution overall. Another feature that was moved to Simulink which the controller could handle itself is dead time for the IGBTs. The current code has dead time from simulink blocks, which works, but would have been handled better by the enhanced PWM feature of the controller. The enhanced PWM feature also requires the PWM output ports to match, where for example PWM1A and PWM1B would control a single leg of the IGBTs. This is not how the board is set up currently and would require some cables to be crossed to work.

If one were to reorder the converter PCB from the manufacturer, one could potentially save a lot of time by fixing the controller slot so it fits. One could also move the optocouplers onto the converter PCB. This would be benefitial because you avoid the need for many jumper wires between boards which can potentially complicate the process of putting it all together. One could also reroute the PWM signals so that the pairs match the IGBT legs for the reasons mentioned.

8.2 Design Corrections

Some small prototyping mistakes in the design remained at the end because shipping and production of the boards were slower than expected, and there was not time for new orders. These flaws are mostly because of limited PCB experience but does not change the functionality of the board itself. The most noteworthy is related to the surface mounted operational amplifiers in the scaling circuits. Some of the pads of these components ended up on the bottom layer instead of the top layer. This problem was solved by soldering jumper wires from the legs of the component to nearby resistor leads. The holes for the resistors were barely big enough to fit the resistor leads together

with the smallest wire found at the university lab. Since discovering this problem, the files that were used to order the PCBs has been corrected, so this issue would not exist if one were to reorder the PCBs.

8.3 Future Work Recommendation

Because of a lack of time, the final steps needed to do tests on real hardware were not completed and have been left for someone else to continue. This means that future work mainly consists of putting the pieces together and verifying that the control system operates properly on real hardware.

There are three main things I would have liked to work more on while working on this thesis.

1. Solve the hardware issues and improvements mentioned in 8.1. This would increase the quality of the lab model and make it aesthetically look better.
2. Investigate different measurement circuits to see if there is one that is more compact. This would make it much easier to move everything to a single PCB. For example one which uses a shunt resistor might be a better solution for a task like this where the rotor power is low.
3. Verify the control system on real hardware and test that the system is stable and working correctly. This could also include looking at the harmonic distortion from the converters and researching if it is a problem and if a filter would be required at this small scale. Power loss and cooling requirement is also something one needs to verify what is necessary.

Chapter 9

Conclusion

In this thesis, a description for creating a small scale DFIG system has been described. The DFIG system is divided into separate circuit boards and components which all are interconnected and presented in a prototyping stage. The most complicated aspect of a DFIG is the converter between the rotor of the generator and the grid. The converter uses small IPMs which is controlled by the C2000 Delfino F28379D LaunchPad from Texas Instruments to generate PWM signals for the IGBTs. The Texas Instruments controller samples signals such as rotor position, rotor speed, grid voltage, DC bus voltage, current into the converter and rotor current for use in a control system which regulates the DFIG. The voltage and current signals have been scaled to fit the requirement of the controller's analog signal input ports.

The boards themselves have not been tested and have some minor design mistakes that makes working with them messy. Therefor they serve better as boards to verify the performance of the individual boards and methods, and not as a complete system. While it should in theory be possible to build it into a complete DFIG lab model, it is likely better to make certain changes outlined in chapter 8, and then progress to the next step.

A simulation of a DFIG has also been used to demonstrate the torque response and regulation of a DFIG. The DFIG in the simulation is a 2MW turbine which is controlled by a maximum power point tracking method called indirect speed control and current loops for space vector PWM. The result of this simulation is a reference for how the lab model should respond,

and the control program has been adapted into a simulink program which can generate code for Code Composer Studio using an embedded coder function in Simulink.

Using motor parameters which are similar to those of the lab DFIG, a Matlab program which outputs the steady state performance of the DFIG has been used. This is useful when prototyping a DFIG, as you have performance characteristics of a similar generator which you can use as a comparison when verifying that your design works as intended.

Future work and recommendations on this project has been outlined in detail in chapter 8.3, and will include verifying the current design, making improvements where there is potential and putting it all together into a complete lab model where future experiments linked to the performance of the generator can take place.

Bibliography

[1] *History of wind power - U.S. Energy Information Administration (EIA)*, https://www.eia.gov/energyexplained/wind/history-of-wind-power.php.

[2] *Wind energy*, en, /wind.

[3] *GE's Haliade-X 14MW turbine to debut at third phase of world's largest offshore wind farm - equinor.com*, no, https://www.equinor.com/no/where-we-are/united-kingdom/doggerbank-18-december-2020.html.

[4] H. Abu-Rub, M. Malinowski, and K. Al-Haddad, "Power Electronics for Renewable Energy Systems, Transportation," p. 827,

[5] L. Sivertsen, *Elektriske Maskiner, Oppbygning, virkemåte og drift*, Norwegian, First. Fagboksforlaget, 2019, ISBN: 978-82-450-3296-3.

[6] *By Nagle - Own work, CC BY-SA 4.0, https://commons.wikimedia.org/w/index.php?curid=46590664*.

[7] "Doubly Fed Induction Machine Modeling and control for Wind Energy Generation," en, in *Doubly Fed Induction Machine*. Hoboken, NJ, USA: John Wiley & Sons, Inc., Sep. 2011, pp. i–xiv, ISBN: 978-1-118-10496-5 978-0-470-76865-5. DOI: 10.1002/9781118104965.fmatter.

[8] K. Blecharz and M. Morawiec, "Nonlinear Control of a Doubly Fed Generator Supplied by a Current Source Inverter," en, *Energies*, vol. 12, no. 12, p. 2235, Jan. 2019. DOI: 10.3390/en12122235.

[9] A. Sagedal, "Design of rectifier system for electric ferries," eng, Jun. 2018.

[10] *TI LaunchPad F28379D Datasheet*, https://www.ti.com/lit/ds/sprs880o/sprs880o.pdf?ts=1622369092311.

[11] *What is MATLAB?* en, https://www.mathworks.com/discovery/what-is-matlab.html.

[12] Mondragon Unibertsitatea and G. Abad Biain, *DFIM Tutorial 2 - Steady-State Analysis of DFIM in Matlab-Simulink*, Apr. 2017.

[13] V. Kazakbaev, V. Prakht, V. Dmitrievskii, M. Ibrahim, S. Oshurbekov, and S. Sarapulov, "Efficiency Analysis of Low Electric Power Drives Employing Induction and Synchronous Reluctance Motors in Pump Applications," en, *Energies*, vol. 12, no. 6, p. 1144, Mar. 2019, ISSN: 1996-1073. DOI: 10.3390/en12061144.

[14] Mondragon Unibertsitatea with Gonzalo Abad Biain and G. Abad Biain, *DFIM Tutorial 1 - Implementation and Control of a DFIM in Matlab-Simulink*, Apr. 2017.

[15] J. Silva, R. Oliveira, S. Silva, B. Rabelo, and W. Hofmann, "A Discussion about a Start-Up Procedure of a Doubly-Fed Induction Generator System," Jan. 2008.

[16] Mondragon Unibertsitatea and G. Abad Biain, *DFIM Tutorial 3 – Wind Turbine Model based on Doubly Fed Induction Generator in Matlab-Simulink*, Apr. 2017.

[17] *MV1007-405 Induction Motor Slip Ring - Terco [English] MV1007-405 Induction Motor Slip Ring*, en-GB.

[18] Dynapar, *Incremental Encoders | The Ultimate Guide | Dynapar*, en, https://www.dynapar.com/technology/encoder_basics/incremental_encoder/.

[19] S. B. Santra, K. Bhattacharya, T. R. Chudhury, and D. Chatterjee, "Generation of PWM Schemes for Power Electronic Converters," en, in *2018 20th National Power Systems Conference (NPSC)*, Tiruchirappalli, India: IEEE, Dec. 2018, pp. 1–6, ISBN: 978-1-5386-6159-8. DOI: 10.1109/NPSC.2018.8771819.

[20] B. Fortman, "C2000™ MCUs enable the next generation of low-cost, dual-axis servo drives," en, p. 13, 2020.

[21] *TI LaunchPad LAUNCHXL-F28379D QuickStart*, https://www.ti.com/lit/ml/sprui73a/sprui73a.pdf?ts=1620885292165.

[22] *LEM LV 25-P Datasheet*, https://www.lem.com/sites/default/files/products_datasheets/lv_25-p.pdf.

[23] *LA 100-TP Datasheet*, https://www.lem.com/sites/default/files/products_datasheets/la_100-tp.pdf.

[24] *IPC-2221 Generic standard on printed board design*, 2012.

[25] *IGBT Module 6MBP15XSF060-50*.

[26] *Fuji IPM Application manual.pdf*, Dec. 2016.

[27] M. Salcone and J. Bond, "Selecting film bus link capacitors for high performance inverter applications," en, in *2009 IEEE International Electric Machines and Drives Conference*, Miami, FL, USA: IEEE, May

2009, pp. 1692–1699, ISBN: 978-1-4244-4251-5. DOI: 10.1109/IEMDC.2009.5075431.

[28] W. Fosse, K. Fossmo, and S. Elhabbach, *Utvikling av DC-AC vekselretter ved bruk av Hardware-In-The-Loop maskin*, 25.05.20.

[29] *CNY17F Optocoupler Datasheet*, http://www.farnell.com/datasheets/2046571.pdf.